POLITECNICO DI TORINO

Corso di Laurea Magistrale
in Ingegneria per l’Ambiente e il Territorio

Soil contamination by heavy metals: laboratory tests and numerical modelling of Al and Zn transport in unsaturated porous media

Relatore

Prof.ssa Tiziana Tosco

Co-relatori

Prof. Roberto Revelli

Prof. Rajandrea Sethi

Ing. Monica Granetto

Candidata

Paola Piarulli

Anno Accademico 2021/2022

Abstract

Soil pollution is of great environmental concern. Particular attention must be focused on urban areas, where heavy metals represent the key contaminants as a result of mainly anthropic activities. Under the evidence of their negative impacts on human health and ecosystems, environmental research is now working on reconstructing the fate of such elements, studying their behaviour during transport across soil layers. In the present thesis work, a small-scale approach has been adopted, with column and batch tests that investigated two target contaminants, zinc and aluminium. These two elements have been studied in the form of Zn(II) and Al(III) chloride solutions.

The two selected elements have been analysed with UV-vis spectrophotometry technology. Moreover, to gain more consistent quantitative results, analytical detection methods were developed through colorimetric reagents. The developed method, different for zinc and aluminium, is based on the complexation reaction between the metal and a selective dye analyte. The formed complex takes on a characteristic colour that can be effectively detected in the visible spectrum. Zincon and pyrocatechol violet are the two ligand agents used for zinc and aluminium detection, respectively. The absorbance measurements have been done at 620 and 573.5 nm, where the linear correlation between absorbance and concentration was best expressed.

Fate in saturated and unsaturated conditions for each contaminant has been studied on the same column, in succession. The results, analysed in terms of breakthrough curves (BTCs), were subsequently modelled with the HYDRUS-1D software. Sand-packed column saturated tests showed no retardation of both zinc and aluminium paths. Slight retention (10 – 20 %) on the contrary is observed. These results were confirmed by experiments in unsaturated conditions, apart from the aluminium that shows an unexpected behaviour. A similar result in terms of retention is obtained with column tests on standard soil, which however show a marked delay in contaminants' BTCs. Batch adsorption tests for both contaminants showed that the amount of element adsorbed onto soil increases by increasing the initial concentration with a linear and a IV-type isotherm for aluminium and zinc, respectively. To simulate a real contamination, a final experiment has been conducted with a pulse injection of zinc-enriched material on a sand-packed column.

The study indicates the general tendency of contaminants to spread deep. This could mean groundwater pollution. Note, however, that in sand material they seem to behave almost like non-reactive solute, while sorption mechanisms in soils can slow down the spread. New studies can be done on the topic, involving other contaminants' concentrations and larger analytical scales.

Contents

1 Introduction

Urban contamination is causing increasing interest and global concern for the magnitude it has acquired in recent decades. One of the main factors to consider is the process of urbanization, namely the *'socio-economic process that transforms the built environment, converting formerly rural into urban settlements, while also shifting the spatial distribution of a population from rural to urban areas'* according to the last World Urbanization Prospect by the United Nations (UN DESA, 2019). The rate of urbanization is increasing. By 2030, 60 per cent of the world's population will live in urban areas, reaching 68 per cent in 2050. This trend will affect all the continents with a boost from North America, Latin America and the Caribbean, where 90 per cent of the population will live in urban areas. Europe will reach 85 per cent. The Asian and African continents exhibit a constant growth, with 59 and 66 per cent urbanization rates by mid-century, respectively. Oceania, bucking the trend, will keep the ratio of rural to urban population unchanged, going from 70 per cent to slightly higher values (UN DESA, 2019).

Urbanization appears directly related to increased contamination levels in urban areas because of human activities. Cities are, in this sense, sources of point and nonpoint emissions from industries, residential activities, transport, power generation, heating and cooling systems, waste management and other activities. Such releases, intentional or unintentional, make the urban zone a sink for a series of contaminants in each environmental compartment. This is a globally increasing threat for its implications on human health and ecosystem services, also considering the urban-rural contamination gradient that can generate.

The soil compartment has a double role among contamination processes, firstly as a place of direct contamination from anthropic pressures (by deposition and discharge) and secondly as a vehicle of pollution for groundwater systems, through the infiltration of dissolved contaminants. However, interaction mechanisms between soil and reactive solutes play a protective role against groundwaters, slowing down or preventing the contaminants spreading. This leads to increased topsoil contamination with respect to the subsurface and the groundwaters. This last aspect suggests the importance of deepening the studies on the unsaturated zone (also called the *vadose zone*). This region is not yet properly investigated since its complexity would require a multidisciplinary approach. The present thesis focuses on this area, trying to evaluate the interaction with contaminants.

Most of the elements in anthropogenic emissions are found to be potentially toxic elements (PTEs) and organic pollutants, such as polycyclic aromatic hydrocarbon (PAHs). PTEs are heavy metals with potentially toxic effects on human health and the environment. The most commonly PTEs retrieved in urban soil as anthropogenic pollutants are Pb, Cd, Cu, Zn, Hg, Cr, Co, Ni and Al. Many soil contamination situations by heavy metals in an urban context are reported in the literature. Comparison with background values or from previous samplings necessarily leads to a direct link with human action. The same trend is observed in different areas of the world (Europe, China, South America, Iraq) although with different magnitude in developing contexts (Imperato et al., 2003; Wei and Yang., 2010; Trujillo-González et al., 2016; Li et al., 2007; Khorshid and Thiele-Bruhn, 2016). In particular, these studies present as indicators of urban soil pollution the contaminants Cd, Pb, Zn and Cu generally found in increasing quantities moving from rural areas to areas with a high rate of industrialization. All these metals are related to traffic, road conditions, tire and brakes wear, lubricants, and paints and fuels (García-Martínez and Poleto, 2014; Kamani et al. 2015). Not the same for Al, Cr and Ni, whose presence is often due to lithogenic origin (Pavlovic et al., 2021). To give some quantitative elements, Al accounts for the 7.2 and 8.2 per cent in granitic and basaltic rocks respectively (Bradl, 2005). Consequently, the development of effective strategies to manage heavy metal pollution is of great importance but requires extensive knowledge of the sorption and transport behaviours of heavy metals and of the diverse variables affecting these processes (Fonseca et al., 2011).

In this thesis, the investigated contaminant species are Aluminium and Zinc, two metals widely used in industrial production. As metals, their toxicity is not simply linked to their presence but to the tendency to dissolve and mobilize according to delicate balances, regulated by pH, redox potential, competitive sorption etc. These parameters govern metals precipitation, redissolution and sorption-desorption. With batch and column tests, the aim of this thesis is to develop an easily applicable analytical procedure for their detection in soils and water, and to describe their behaviour in unsaturated soil after a preliminary characterization in saturated conditions. In the following sections an overview of Aluminium and Zinc – their presence nature, the reasons why it is important to control their spread in the environment is reported.

Aluminium contributes about 8 per cent (by weight) to the Earth's crust, which makes it the most abundant metal and the third element of the lithosphere (after oxygen and manganese) (Irsa-Cnr, 2003). Thus, it cannot properly be considered a contaminant. The naturally occurring aluminium is present in combined form, relatively stable and with limited bioavailability. Under the effect of acidic pH, typical of polluted environments, ionic aluminium is released from its complexed/combined forms (Mesquita and Rangel, 2008). Thus, dissolved Al concentrations increase in acidified soil and surface waters. Free water cations (Al^{3+}) are present at pH 3.5, while at higher pH values cationic hydro complexes $Al(OH)^{2+}$ and $[Al(OH)_2]^+$ are abundant in the water environment (Matúš et al., 2009). The most toxic aluminium species are precisely these positively charged monomeric forms. In recent years, attention has increased to the potential toxicity and morbidity of aluminium. Studies highlight the correlation between human exposure to aluminium with nervous system diseases (Campbell et al., 2004; Flaten, 2001; Zatta et al., 2003) not to mention the known toxic effects on plants and animals (Rahman et al., 2021; Cronan and Schofield, 1979 ;Jones et al., 1998). Given its negative roles for living beings, both the detection of aluminium even at trace levels in the environment and understanding its dynamic have acquired great importance.

Zinc is present in the Earth's crust at a mean concentration of 70 mg/kg (Irsa-Cnr, 2003). Natural soil zinc derives from the weathering of parental rocks. Zn presence becomes significant in granitic and basaltic rocks where it counts for 50 and 118 mg/kg respectively (Bradl, 2005). Anthropic Zn presence in urban soils is due to industrial and mainly transportation activities, as mentioned before. Zn is an essential element for humans, plants, and animals, but when at quantities exceeding the required ones, it can produce toxic effects. Soil zinc toxicity in the environment – phytotoxic effects or water contamination – depends on its concentration in soil, determined in turn by sorption-desorption mechanisms, colloids presence and competitive sorption (Fernández-Calviño et al., 2010). Mason et al., 1999, in a study on the behaviour of roof run-off elements during infiltration through the soil, demonstrate the tendency of Zn to go deeper and deeper in soil layers of the unsaturated zone. All these reasons have been lately prompted studies on Zn as a contaminant.

Contaminants' behaviour has been addressed with batch and column tests, in order to evaluate two interconnected aspects, sorption and transport processes. Transport tests have been carried out in sand columns, at a constant flow rate, as a first step. After evaluating metals' tendency to be adsorbed in soil batch tests, soil-packed column tests have been performed. Results have been analysed in terms of breakthrough curves – variation of concentration over time – and in terms of sorption isotherm – variation of soil sorption capacity with respect to concentration at equilibrium.

To perform these tests and obtain quantitative results, an analytical detection method for Al and Zn has been developed, easily applicable and able to provide accurate and meaningful results of Al and Zn concentrations. The traditional techniques for metals' determination (FAAS, GFAAS, ICP-OES and ICP-MS) even though provide high selectivity, are expensive in terms of both instrumentation and operating costs. For this work, a less sophisticated, but equally relevant approach has been used to perform analysis with a simpler apparatus, namely UV-vis spectrophotometry using colorimetric reagents. The method is based on the metal-dye reaction to form a coloured complex that exhibits an absorbance peak at a specific wavelength (λ) of the visible spectrum. Methods from the literature were used as the basis to define simplified protocols, simpler and with fewer reactants used, improving the safety of users and the environment For zinc, the method involved the use of Zincon (2-carboxy-2-hydroxy-5-sulfoformazylbenze) as a ligand agent. The formed Zn(II) – Zincon complex presented a reddish colour, less intense going toward less concentrated Zn(II) solutions. The absorbance values for pH 10.6 solutions were recorded at 620 nm, where the calibration line of the complex solution showed good linearity. Aluminium was detected using Pirocathecol Violet (PV, $C_{19}H_{14}0_7S$). The Al(III) – PV complex at pH 6.8 gave a maximum absorbance at 573.5 nm.

This thesis is structured in five chapters. Their content is briefly explained in the following:

CHAPTER 2 – BACKGROUND LITERATURE: the theoretical background on general soil-water concepts, water flow and solute transport in saturated and unsaturated conditions is presented in the first part. A second section is dedicated to the currently used methodologies for metals detection, with a focus on the metals object of the study.

CHAPTER 3 – MATERIAL AND METHODS: it includes a description of the set-ups used during the experimental study with detailed information on methods for the execution of the tests, analysis and modeling of the results using the software HYDRUS-1D (input parameters, BC and IC to set).

CHAPTER 4 – RESULTS AND DISCUSSION: the results of all the performed tests are presented, with a brief discussion. Sorption isotherms from batch tests and breakthrough curves from column tests on sand/soil material are described.

CHAPTER 5 – CONCLUSIONS: conclusions of the work are reported, with some elements on future developments.

2 Literature background

2.1 Transport in saturated and unsaturated conditions

2.1.1 Water infiltration

Infiltration occurs under the effect of the gravity force and the capillarity phenomenon. Its rate is also controlled by the hydraulic conductivity K of the soil. Consequently, water infiltrates according to a series of factors: soil properties, moisture content, precipitation rate; all these elements determine the infiltration rate, *f*. Each soil is characterised by an infiltration capacity, f_c, that defines its ability to absorb water (Tarboton, 2003).

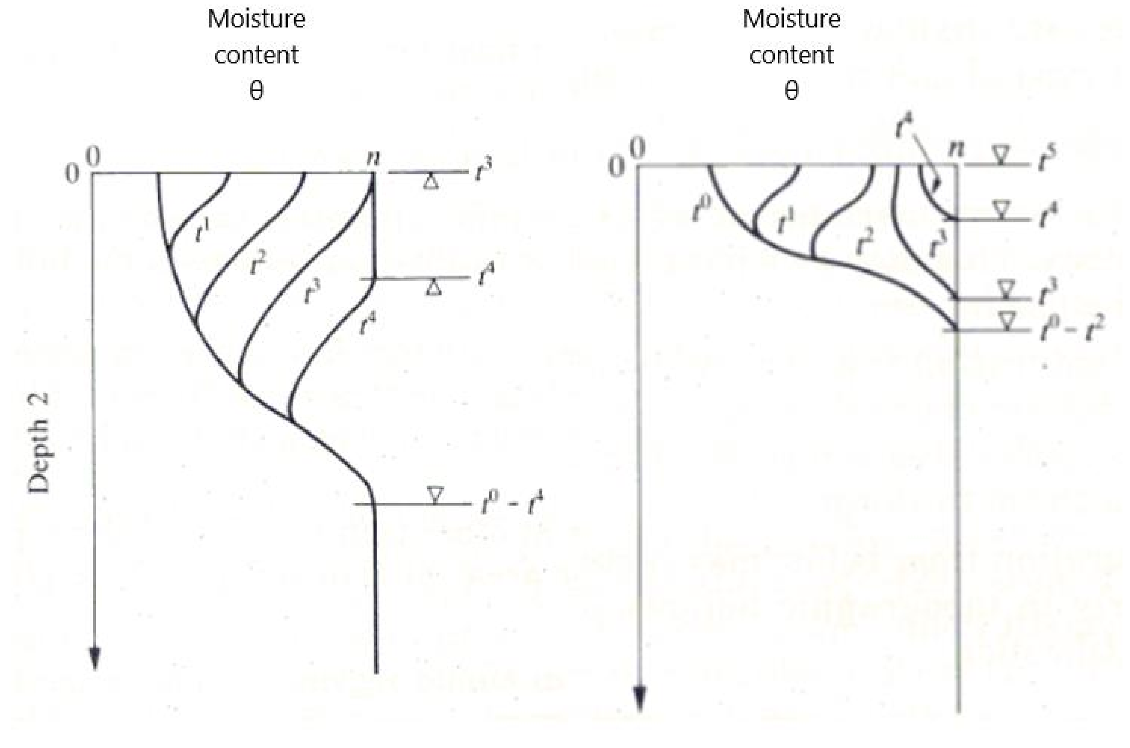

a) *b)*

Figure 2.1 - a) Infiltration excess runoff generation mechanism; b) Saturation excess runoff generation mechanism (modified from Tarboton, 2003)

A rainfall phenomenon determines a water accumulation on the surface, increasing the hydraulic load Δh relative to the bottom. Due to this generated gradient, water starts flowing across soil layers. By comparing the rain intensity *w (L/T)* with the hydraulic conductivity at saturation K_s *(L/T)*, two different behaviours are shown.

In particular:

- If $w < K_s$

Water infiltrates across layers at a lower rate than that at which the upper layer is saturated. At this time (ponding time), as the rain intensity equals the infiltration capacity, runoff is generated. From now on, the wetting front begins to deepen reaching the piezometric surface and the infiltration stops.

The overall phenomenon consists of a progressive reduction of the infiltration capacity in time, which corresponds to an increase in runoff (Tarboton, 2003).

- If $w > K_s$

The vertical water flux infiltrates at a higher rate than the top layer saturation velocity. The water table is met before top layer saturation is reached. Since this moment, going on the precipitation, the piezometric surface rises until reaching the top layer. From now on all further surface water input becomes runoff.

This process is known as the *infiltration excess process*. In Figure 2.1 the two described situations are schematized.

Several models have been developed in time to study the infiltration mechanism. Some have an empiric nature, like the SCS-CN method, a one-parametric model based on soil type, land use and precipitation. Others, such as the Horton or the Green-Ampt models are physical simplified models and describe the decreasing of the infiltration capacity during a storm as a function of cumulative infiltrated depth and time, respectively (Tarboton, 2003).

Water that infiltrates in a porous medium moves within pores formed by the solid granular frame. A porous medium is formed by a solid matrix, with voids that can be filled by water and/or air. The flow may occur in saturated or unsaturated conditions depending on whether water fills the pores or not. Indicating with θ (-) the water content and with ϕ (-) the porosity, it can be schematically stated that the first situation emerges when $\theta = \phi$, the other when $\theta < \phi$. The relations describing these two quantities are reported below:

$$\phi = \frac{Volume\ of\ voids}{Total\ volume} \tag{2.1}$$

$$\theta = \frac{Volume\ of\ water}{Total\ volume} \tag{2.2}$$

The parameter that relates them is the degree of saturation S (-), defined as:

$$S = \frac{\theta}{\phi} \tag{2.3}$$

Hence, S = 1 indicates saturated conditions; for unsaturated soils, the degree of saturation varies between 0 and 1 (Tarboton, 2003).

Fluid flow in porous media can be described by the single-phase flow equation set out by Darcy:

$$q = -K\left(\frac{dh}{dz}\right) \tag{2.4}$$

Where: K (L/T) is the hydraulic conductivity; ρ (M/L^3) is the water density; g (L/T^2) is the gravitational acceleration; h (L) is the hydraulic head and dh/dz is the (vertical) hydraulic gradient, i (-).

At a macroscopic scale, the *specific discharge q (L/T) or Darcy velocity* is defined as:

$$q = \frac{Q}{A} = -K\frac{\Delta h}{\Delta z} = -Ki \tag{2.5}$$

where Q ($L^3\ T^{-1}$) is the flow rate; A (L^2) is the cross-sectional area.

The hydraulic conductivity of a medium K describes the amount of water that can move through pore spaces or fractures. Thus, K depends on a series of factors, mainly filled pores (size and shape) and interconnected channels within the porous medium. In unsaturated media, K is strongly influenced by the water content: a reduction in the water content makes the larger pores empty first. Moreover, the subsequent grains rearrangement reduces the size of the pores. These factors combine to reduce K as with fewer smaller pores filled, the paths of water flowing through the medium become more tortuous. Passing from saturated to dry conditions the loss of hydraulic conductivity can be of various orders of magnitude (Nimmo, 2005).

2.1.2 Solute transport

The description of solute transport in the soil is of interest for example to quantify salt displacement in salt-affected soils, pollutant mobility (heavy metals, excess fertilizer, pesticides, and radionuclides), and the mobility of plant nutrients (van der Zee and van Riemsdijk, 1987). Assuming that the contaminant flow in the vadose zone can be described by the same mechanisms of propagation that are valid in saturated conditions, our discussion will start from the transport in saturated porous media.

2.1.2.1 Propagation mechanisms in saturated porous media

The following description follows Sethi and Di Molfetta (2019).

The processes involved in solute transport in a porous medium are classified as hydrological, chemical-physical, biological. They are simultaneous processes in a system, but they can be more or less relevant according to the system's nature and the contaminant type.

Hydrological processes include advection, molecular diffusion and cinematic dispersion. Among these, advection is the most significant.

According to advection, the contaminants are transported in the water flux direction with the same effective velocity, v_e, of the water flux. The effective velocity is the average velocity of water passing through connected pores:

$$v_e = \frac{q}{\phi_e} = \frac{Ki}{\phi_e} \tag{2.6}$$

where ϕ_e (-) is the effective porosity. The mass flux of contaminant in the flow direction is only due to advection; the process is described by the following equation:

$$j_A = v_e \phi_e C \tag{2.7}$$

where C (M L^{-3}) is the solute concentration. Advection does not consider dispersion phenomena responsible for dilution and mass exchanges across the tubular channel of contamination. Such aspects are considered in molecular diffusion and cinematic dispersion mechanisms, both microscopical phenomena.

Molecular diffusion is related to the chaotic motion of the solute molecules: collision among molecules results in an overall movement from higher to lower solute concentration zones. The mass flow of contaminants is proportional to the concentration gradient, and it is described by the Fickian law.

Cinematic dispersion is determined by the heterogeneity of the porous medium that creates a velocity profile within each pore: higher values are detected at the centre and a zero value on the pore walls; moreover, the velocity in the midline differs across pores of varying sizes. In addition, the tortuosity of the flow path induces a transversal component of the velocity that leads to the spreading of the contaminated zone. To simplify these complex phenomena a Fickian model is used, as seen for molecular diffusion.

Due to the similarity in their analytic description, these two last propagation mechanisms converge in a single process defined by the relation:

$$j_I = -D_L \frac{\partial C}{\partial x} \tag{2.8}$$

where D_L ($L^2 T^{-1}$) is the hydrodynamic dispersion coefficient in the direction of the flux. It includes both molecular diffusion and cinematic dispersion, as shown by the following equation:

$$D_L = D_0 + D_C = D_0 + \alpha_L v_e \tag{2.9}$$

where D_0 and D_c ($L^2 T^{-1}$) are representative of the molecular diffusion and cinematic dispersion, respectively, while α_L is the longitudinal dispersivity and has the dimension of a length. Depending on the water velocity we can have a dominant advective or diffusive transport. Hence, eq. 2.9 can be simplified neglecting the first or the second dispersion coefficient. For typical velocity values of aquifer groundwater systems, cinematic dispersion is the prevalent mechanism, thus the relation can be modified as follows:

$$D_L \approx \alpha_L v_e \tag{2.10}$$

The transverse components of dispersion coefficient and dispersivity (D_T and α_L) are related in the same way; in general, the lateral dispersivity is smaller than the longitudinal one by one to two orders of magnitude (Dagan, 1984). In fact, α_L controls the movement of the plume in the mean flow direction, while α_T governs the lateral spreading of the plume, which in general is less consistent. α_L is a scale-dependent parameter, it depends on the mean travel distance or distance along with the movement of contaminant transport in porous media, with higher values for a higher extent of contamination phenomena. The scale effect is due to spatial heterogeneities.

Chemical and biological processes influence solute propagation when it comes to reactive solutes. They consist mainly of chemical reactions, mediated or not by microorganisms, that lead to the elimination or transformation of contaminants with the generation of reaction products (radioactive decay, redox reactions, precipitation, dissolution, etc.). Reactions are generally described by first-order kinetics.

For biodegradation, Monod proposed a more rigorous model considering the substrate (contaminant) concentration as a limiting factor to the microorganisms' growth:

$$\frac{dC}{dt} = -\mu(C)C = -\mu_{max}\frac{C}{K_c + C} \tag{2.11}$$

where μ *(T^{-1})* is the growth rate of microorganisms; μ_{max} *(T^{-1})* is the maximum growth rate of microorganisms; C *($M\ L^{-3}$)* is the contaminant concentration; K_c *($M\ L^{-3}$)* is the semi-saturation constant.

A problem in the practical applicability of Monod's model is the estimation of all these parameters, therefore the first-order kinetic is the most adopted model.

Radioactive decay is described as follows:

$$\frac{dC}{dt} = -\lambda C \tag{2.12}$$

Where: λ *(T^{-1})* is the decay constant and it is related to the half-life $t_{1/2}$ by the relation:

$$\lambda = \frac{0.693}{t_{1/2}} \tag{2.13}$$

Physical-chemical processes (sorption processes) are involved during the interaction solute-solid matrix. Sorption can happen as ion exchange, adsorption, absorption or chemisorption. Adsorption in a strict sense does not involve chemical reactions at the solid-liquid interface; thus it is a reversible process of contaminant transferring from liquid to solid phase. At a macroscopic scale, it results in retardation in the propagation of the contaminant, measured by the R factor *(-)*:

$$R = \frac{v_e}{v_c} \tag{2.14}$$

For adsorption processes described by a linear isotherm ($S = K_d C$), R is expressed as:

$$R = 1 + \frac{\rho_b}{\Phi_e}K_d \tag{2.15}$$

Where: ρ_b $(M\,L^{-3})$ is the bulk density; ϕ_e (-) is the effective porosity; K_d $(M^{-1}L^3)$ is the solid-liquid partition coefficient.

For adsorption processes described by a Langmuir isotherm ($S = \frac{\alpha\beta C}{1+\alpha C}$), R is expressed as function of the concentration, according to:

$$R = 1 + \frac{\rho_b}{\phi_e}\left(\frac{\alpha\beta}{(1+\alpha C)^2}\right) \tag{2.16}$$

Where α (L^3M^{-1}) is the Langmuir sorption equilibrium constant and β (MM^{-1}) is the maximum sorption capacity.

All these components considered, the differential equation of mono-dimensional dispersion for reactive solute can be written as:

$$D_L\frac{\partial^2 C}{\partial x^2} - v_e\frac{\partial C}{\partial x} - \lambda C = R\frac{\partial C}{\partial t} \tag{2.17}$$

2.1.2.2 Unsaturated porous media

The unsaturated zone plays several critical hydrologic roles. Such hydrological processes involve the movement of water, air, solid. That is the reason why transport in an unsaturated medium is often referred to as 'multiphase' flux (Nimmo, 2005).

For its specific nature, the unsaturated zone involves several difficulties. As a first aspect, forces acting on vadose water cannot be restricted to earth's gravitational field forces, as it generally is for groundwater (Nielsen et al., 1986). The other significant type of energy determining retention in an unsaturated medium arises from the interaction of water with the rigid matrix. (Nimmo, 2005). In the unsaturated zone, water in the pores is subject to surface-tension forces that are responsible for a negative pressure head ψ (or matric head), also referred to as suction head (Van Genuchten and Pachepsky, 2011). Opposite condition in saturated soils, where ψ is positive, while at the water table ψ = 0.

To conclude, from the definition of suction head, water in small pores is held under a higher tension relative to larger-sized pores: the suction head is proportional to pore channel perimeter over the channel area. Put differently, the height of capillary rise is greater for small channels, proving that the water content is a function of the suction head.

The soil-water retention curve θ(h) describes the relationship between the water content and the energy status of water. It is also known as capillary pressure-saturation or soil moisture characteristic curve (Van Genuchten and Pachepsky, 2011). In Figure 2.2, characteristic curves for different types of soils are represented. Coarse soils exhibit a step-like characteristic curve since water content drops rapidly at a small suction head. As the material becomes fine-textured, the shape of the curves tends to be more sub-vertical, indicating a water content gradually lost, also for high suction heads.

As indicated in the x-axis, the water content ranges between a maximum value, θ_s related to saturated conditions and a minimum value θ_r, representing a residual or irreducible water content. This last value differs from 0 because of the presence of trapped-non drained water (van Genuchten and Pachepsky, 2011). For such value, the pressure head tends asymptotically to infinite.

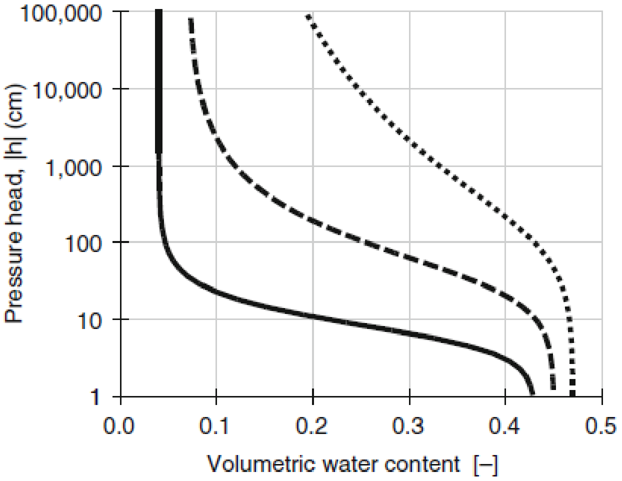

Figure 2.1- Typical soil water retention curves for coarse (solid line), medium (dashed line) and fine-textured (dotted line) soils (From van Genuchten and Pachepsky, 2011*)*

The pressure head tends to 0 for a volumetric water content approaching the saturation value θ_s. For θ equal to θ_s the water content cannot further increase its value, so the curve presents an inflection point (bubbling point). This point, characteristic for each system, represents a threshold capillary pressure that air must overcome to start the water displacement.

Soil-water retention curves are not unique, there is not a ψ-θ (or ψ-K) two-way relationship. They depend on the history of the soil. The wetting curve does not follow the same trend as the drainage. In particular, for a given pressure head, the water content is higher for the drainage curve relative to the imbibition curve. This displacement refers to as hysteretic behaviour. At least three situations contribute to generating hysteresis: ink-bottle effect, due to not uniform pore dimensions; air trapped during wetting; swelling/shrinking phenomena. An example of the hysteretic nature of θ (or K) in function of ψ is reported in Figure 2.3. As we can see, $\theta(\psi)$ and $K(\psi)$ exhibit a similar trend, while in general, $K(\theta)$ – θ as independent variable – shows a less pronounced, but not necessarily negligible for all soils, hysteretic shape (Nielsen et al., 1986). Hysteretic phenomena are described in more detail in Figure 2.4. In the same graph, the influence of entrapped air is highlighted.

The curve that begins at one hundred per cent water saturation to residual water saturation is called the main drainage curve. In contrast, the main imbibition curve begins at residual water saturation and continues until theoretically complete saturation. When trapped air is present, the final water content (at zero pressure head) will be other than 1, as depicted in the figure. These two curves define the hysteresis envelope, which contains an infinite number of possible wetting/drying *scanning curves* depending on where imbibition/drainage begins (dashed lines). For example, a drainage curve starting along the main imbibition branch is referred to as *a primary drainage scanning curve*. *Secondary scanning curves* may be initiated at reversal points on a primary scanning path and so on for higher-order scanning curves (Bear and Cheng, 2010).

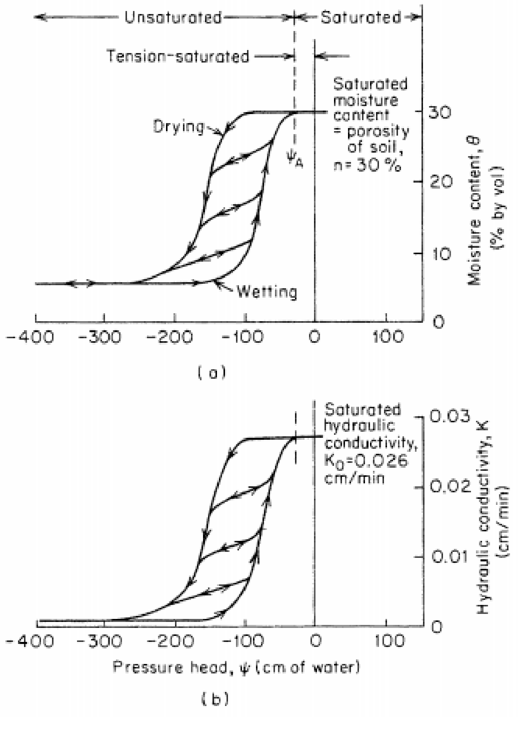

Figure 2.3- a) $\vartheta(\psi)$ characteristic curve; b) $K(\psi)$ characteristic curve. From Freeze and Cherry (1979)

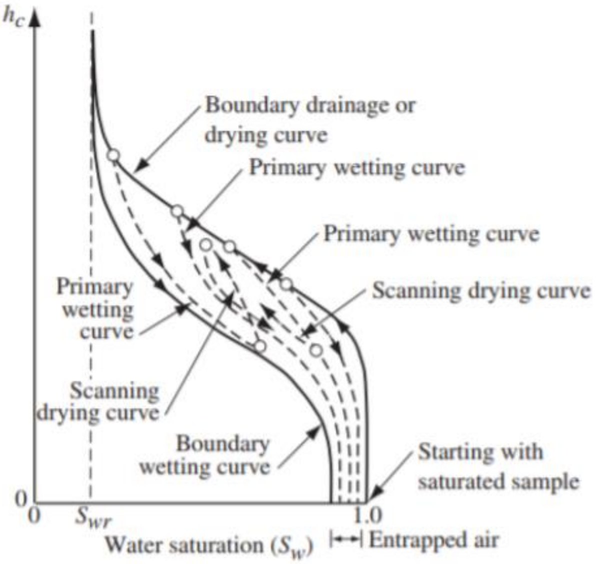

Figure 2.2- Hysteresis in a capillary pressure curve (from Bear and Cheng, 2010*)*

A series of models have been proposed to describe the soil-water characteristic curve θ(h) and the hydraulic conductivity function K(h) or K(θ). The analytical representations are based on theoretical pores-size distribution models by Burdine, 1953)or Mualem (1976) that approximate the soil with capillary tubes containing and transmitting water (van Genuchten and Pachepsky, 2011).

Examples of θ(h) and K(h) empiric equations are the hydraulic functions by Brooks and Corey (1964) and van Genuchten (1980), which use Burdine's and Mualem's theory, respectively.

Brooks and Corey's empirical equation provides sufficiently accurate predictions, especially for coarse soil with relatively narrow pore size distributions; in the case of soils with a large range of pore sizes instead, it gives a poor fit with observed retention data close to saturation. It presents a marked discontinuity in correspondence of a specific air-entry value h_e (related to the bubbling pressure), which ignores the presence of a transition zone at and near the bubbling pressure (van Genuchten and Nielsen, 1985). Van Genuchten, 1980 has suggested a more realistic S-shaped model, with a smoother path near saturation. The equation is given by:

$$\theta(h) = \begin{cases} \theta_r + \dfrac{\theta_s - \theta_r}{(1 + |\alpha h|^n)^m} & h < 0 \\ \theta_s & h \geq 0 \end{cases} \tag{2.18}$$

Where: α (L^{-1}), n (-) and m (-) are shape parameters characteristic of the medium.

Considering the relation valid for the Mualem model:

$$m = 1 - \frac{1}{n}, \quad 0 < m < 1 \tag{2.19}$$

The Van Genuchten-Mualem equation is obtained:

$$K(h) = K_s S_e^l \left[1 - \left(1 - S_e^{1/m}\right)^m\right]^2 \tag{2.20}$$

Where: K_s *(L/T)* is the hydraulic conductivity in saturated conditions; l *(-)* is the pore-connectivity parameter, fixed by Mualem in 0.5 for most soils; S_e *(-)* is the effective saturation. S_e is an important parameter for unsaturated conditions. It quantifies the moisture content in variably saturated soils. It is defined so that the values of saturation vary from 1 to S_r (residual saturation), as follows:

$$S_e = \frac{\theta - \theta_r}{\phi - \theta_s} \tag{2.21}$$

Darcy's equation, originally derived for saturated flows, can be extended to unsaturated conditions in the vadose zone (Nielsen et al., 1986). As mentioned above, the presence of an air phase in the unsaturated zone reduces the value of hydraulic conductivity differently, depending on the local values of water content. Therefore, K in the Darcy equation must be considered as a function of water content. In any case, the general structure of the equation is still valid. The combination of the Darcy and continuity (conservation of mass) equations leads to the Richards equation (Richards, 1931), which describes the vertical movement of water through unsaturated soils. In terms of moisture content, the relationship is expressed as follows:

$$\frac{\partial \theta(h)}{\partial t} = \frac{\partial}{\partial z}\left[K(h)\left(\frac{\partial K(h)}{\partial z} - 1\right)\right] + \phi \tag{2.22}$$

Where: z is the flow direction; ϕ is the water sink/source term (Nielsen et al., 1986).

This is valid under the so-called Richards' approximation. In fact, multiphase system modelling requires a flow equation for each fluid present, having to deal with the mutual interaction between the different components. However, these coupling flow equations can be simplified with appropriate assumptions. This happens for the unsaturated zone, where the air pressure is generally controlled by the atmospheric pressure at the soil-atmosphere interface, which is nearly constant. In addition, a no air-phase pressure gradient in the vadose zone means that the gas-phase pressure remains close to the atmospheric pressure. In conclusion, for a two-phase air-water system, the gas phase can be neglected in modelling the liquid phase flow, stating that the airflow does not affect the water flow (Parker, 1989).

This is realistic if there is continuity in the gas phase, so the air is free to move. For conditions close to saturation in the fine-grained soil, primarily, the generation of airflow resistance leads the assumption to no longer be valid, and a two-phase flow model must be used (van Genuchten and Pachepsky, 2011).

2.2 Metals detection methods

Numerous analytical techniques are available for metals detection. Atomic spectrometry, voltammetry, fluorometry, gas chromatography and UV-vis spectrophotometry are the more established to date, often improved with preliminary selection operations. In the following, a brief description of their operative scheme is reported. Typical applications for Zn and Al in water samples are mentioned, with indications on precision (i.e. relative standard deviation, RSD) and LOD (Limits of Detection), where available. When choosing the optimal procedure, a series of factors must be considered: sample nature, required detection limits, robustness, easy functioning, and handling of the instruments (Tria et al., 2007).

For the present thesis work, spectrophotometric readings have been performed.

2.2.1 Atomic spectrometry

Atomic spectroscopy determines the elemental composition of a sample through the quantification and the characterization of the atoms which compose it. Atomic spectrometry can be classified at least in two ways: according to the type of spectroscopy used or to the atomization source. The former distinguishes between optical and mass spectrometry. Optical spectrometry can be divided in turn into absorption (AAS), emission (AES) and fluorescence spectrometry (AFS).

2.2.1.1 Atomic absorption spectrometry

The atomic absorption spectrometry provides a quantitative characterization of the analyte: a specific wavelength is used to excite isolated atoms from the ground to the excited state. The energy absorbed is measured, giving information on the concentration of atoms in the analyte. AAS can be performed only on medium at gaseous phase, in which atoms are well isolated. Thus, the sample, usually in solution, must be subject to volatilization as a first step, then atomized to disrupt molecules and release atoms at the ground state (atoms cloud). Subsequently, monochromatic radiation is sent to the atomic cloud, causing excitation, which is partially absorbed. The contribution to the absorption is given by the atoms at ground level before excitation. Since only a small percentage of atoms is thermally excited during atomization, a linear relationship between absorption and atoms on the optical path of the radiation (i.e. analyte concentration) exists. In such conditions, atomic absorption follows a similar relation to Lamber-Beer law, valid for molecular absorption, although in a narrow linearity range:

$$A = x \cdot b \cdot N \tag{2.23}$$

Where: A (-) is the absorbance; x (-) is the atomic absorption coefficient; b (L) is the optical path; N is the total number of free atoms.

Depending on the atomization system at least two types of AAS can be distinguished: flame atomic absorption spectrometry (F-AAS) and graphite furnace atomic absorption spectrometry (GF-AAS), where a flame and a graphite furnace are used respectively.

Flame atomic absorption spectrometry

The flame atomization technique is the oldest among AAS techniques and it is still indispensable in any chemical laboratory. The system was for a long time the most widely used technique for metals analysis due to its specificity and selectivity, as well as certain ease of use. Premixed laminar flames are the most commonly used devices. Through a capillary tube, the sample solution is aspirated by the oxidizer (oxidant) into the nebulizer, where it is transformed into aerosol (suspension of fine droplets in a gas phase). Once formed, the aerosol passes into the pre-mixing chamber where it is homogenized with the fuel-oxidant mix. With these two gases as carriers, the sample enters the burner, where the laminar flame produces volatilization and atomization. Premixed flames commonly employ either air or dinitrogen oxide as the oxidant and either acetylene or hydrogen as the fuel gas. The applied temperatures vary in the range 2000-3000 K. The type of flame should be opportunely selected according to the analyte. Air-acetylene flame is suitable for over 30 elements, by adjusting the flame conditions (oxidant-fuel proportion) to create an adequate environment (Moldovan, 2019). Other elements – such as aluminium – can be determined using the dinitrogen-oxide acetylene flame.

The atomization efficiency is affected by compound ionization (Moldovan, 2019). This problem reflects the high LOD in aluminium F-AAS determination, which makes it difficult for direct analysis (45 µg/L even for the nitrous-oxide acetylene flame (Moldovan, 2019). Preconcentration/separation techniques are often necessary as preliminary steps, especially for trace aluminium detection. Frankowski et al., 2010 propose a method that combines F-AAS with high-performance liquid chromatography (HPLC). Other examples are given by Ulusoy et al., 2011 that develop a cloud point extraction (CPE) method for the preconcentration of trace aluminium based on the complex reaction Al(III)-Xylidyl Blue before F-AAS detection. In this last case the LODs fall to 1.43 µg/L.

F-AAS for zinc detection provides for better results with lower limits of detection, in the order of 1-2 µg/L with an air-acetylene flame system (Moldovan, 2019), without preconcentration. Using upstream preconcentration/separation the detection limits get lower. (Tony et al., 1999) proposed an F-AAS-FIA (Flow Injection Analysis) combined method for heavy metals detection in seawater, among which zinc. The samples after pH correction (up to 3 ± 1), was complexed with 5,7-dichlorooxine to adsorb onto the preconcentration column. With this method, the LOD for zinc arrives at 0.5 µg/L. This result is someway confirmed by Carletto et al., 2008 that, for the same preconcentration-detection method (with a different chelating agent, 8-hydroxyquinoline) gain a LOD of 0.8 µg/L.

Graphite furnace atomic absorption spectrometry

In GF-AAS the burner system is replaced by a graphite furnace. It consists of a graphite tube, that is heated by resistance in an inactive atmosphere. At a small amount (20-100 µL) the sample is injected into the tube and placed on the optical path of the emitted radiation. The temperature is raised according to a three-stage program, leading in succession to vaporization, incineration (pyrolysis) and atomization. The method is well suited for the analysis of heavy metals in freshwater down the ppb region with good precision (Paus, 1973), reducing by one order of magnitude the detection limits with respect to flame AAS.

GF-AAS applications for aluminium detection present in the literature, report a LOD of 0.1 µg/L on simulated freshwater samples (Epstein et al., 1978). On real seawater samples, Orians and Bruland, 1986 obtained a LOD of 0.1 nmol/L (Tria et al., 2007). The same method reaches 0.4 and 0.5 ng/L limits for zinc quantification in Sturgeon et al., 1979 and Krawczyk et al., 2014, respectively.

As demonstrated by the lower detection limits, GF-AAS has increased sensitivity over F-AAS in measuring metals concentrations in aqueous samples, mainly due to the greater sample residence time, which enables in smaller sample size. Despite these advantages, GF-AAS is affected by a series of drawbacks: matrix interference in high salt content solutions and refractory carbides formation. Chemical modifiers have been largely employed to overcome these problems, i.e. $Mg(NO_3)_2$ in Narin et al., 2004.

2.2.1.2 Atomic emission spectrometry

Atomic emission spectrometry (AES) exploits the opposite phenomenon of AAS: it measures the energy released from the excited atoms when they return to the ground state. High temperatures must be reached to provide the energy necessary for atoms' excitation. A first energy contribution generates sample atomization and an additional energy supply excites the atomic vapour, causing radiation emission.

The primary advantage over AAS is that AES can efficiently handle multi-element analysis since sample atoms are simultaneously excited (Tria et al., 2007). The sensitivity of the method is up to three orders of magnitude higher than AAS.

In AES the excitation can be performed by means of an electric arc or spark (ET-AES), a flame (F-AES) or a plasma. Among the various types of plasma available, the most widely used is the inductive-coupled plasma (ICP), used in ICP atomic emission technique (ICP-AES).

Inductively-coupled plasma-atomic emission spectrometry (ICP-AES)

ICP is a widely used analytical technique for metal detection in environmental samples. Its strong sensitivity makes it particularly suitable for trace metals detection. The first use of inductively coupled plasma as excitation source dates to 1965 with Greenfield (Soodan et al., 2014). From that time, ICP has been improved and modified, leading to developing efficient and automated equipment. In the last twenty years, ICP has become competitive in terms of cost and performance with the traditionally implied atomic absorption methods.

Plasma, described as the fourth state of matter, is defined as highly ionized gas, macroscopically neutral, containing an equal number of electrons and ions. Thus, it is known to be an excellent electrical conductor. To create a plasma external energy must be supplied to the electrons in order to ionize the gas. In this lies the main difference with the flame, which is generated and powered by a combustion reaction. Plasma on the contrary acts as an energy reservoir since it is created and maintained by the energy transfer between an electromagnetic field and a highly ionized gas. Even though from a theoretical point of view any gas can be used as a carrier to generate a plasma, practically noble gases are chosen because of the higher ionization energy, the absence of stable combination with other elements and the simpler emission spectrum due to the monoatomic nature of the vapour (Fernández-Sánchez, 2019). The commonly used gas in ICP is argon (Ar) that ionizes according to the following equation:

$$Ar^0 \xrightarrow{+E} Ar^+ + e^- \tag{2.24}$$

From the operative pattern, plasma emission spectrometry is similar to flame spectrometry: the sample is nebulized and introduced into the source (plasma) where is atomized and excited; the emitted radiations, collected by a monochromator, are sent to the detector.

ICP-AES performances are comparable to those of GF-AAS, but it allows overcoming most of the interferences that affect graphite furnace-based methods. The extremely high temperature (7000 – 9000 K) gives the advantage of minimizing interferences from forming stable refractory oxides elements in AAS (Al included). However, interference cannot be completely eliminated: spectral overlap from elements present in the same sample remains a problem. Aluminium for example emits between 212 and 190 nm, lying in the same region of cadmium, barium and tungsten, as pointed out by Ediger et al., 1980 (Tria et al., 2007).

Successful applications of the ICP-AES method in aluminium and zinc concentration determination are reported in the literature. Rezaee et al., 2010 developed a new liquid-liquid microextraction method to use in combination with ICP-AES aluminium detection techniques in water samples. The final LOD resulted equal to 0.8 µg/L. ICP-AES in zinc determination provides for better results in terms of limit of detection. Zhao et al., 2012 reports a LOD being equal to 0.05 µg/L for a developed separation-detection combined method that uses dual cloud point extraction (d-CPE) followed by ICP-AES on water samples.

Inductively-coupled plasma-mass spectrometry (ICP-MS)

For quantitative measurements, inductively coupled plasma can be effectively coupled with another analytical technique, Mass Spectrometry. The multi-elemental ultra-trace detection capability of ICP-MS makes it a most powerful technique (Beauchemin, 2008).

The analytical sequence of ICP-MS involves specific steps: the sample solution is transferred to a nebulizer by a peristaltic pump. Into the nebulizer, the solution is converted into an aerosol. The aerosol is brought to the centre of the ICP torch by Ar as a carrier gas. As soon as introduced into the plasma, the sample is atomized and ionized, diverting the atoms into the mass spectrophotometer, where they are divided according to the mass-to-charge (m/z) ratio through an electric field, combined or not with a magnetic field. Metal ions are identified from the analysis of the registered mass spectrum. Each spectrometer is characterized by a specific capability to differentiate between masses, usually expressed in terms of resolution R, defined as:

$$R = \frac{m}{\Delta m} \tag{2.25}$$

Where: m is the mass of the ion; Δm is the mass difference between two resolved adjacent peaks.

The major benefits of ICP-MS over ICP-AES are that ICP-MS has the capability of isotope analysis with higher efficiency and lower recognition limits. ICP-MS method is able to detect elemental concentration in the ng/L range (part per trillion).

The limit of detection for ICP-MS application in aluminium detection varies from 3.3 ng/L in Xia et al., 2005, after single drop microextraction, and 0.1 µg/L in Martin-Esteban et al., 1995 where an online preconcentration of aluminium preceded the detection phase in tap water. In this last case, a comparison with F-AAS method is done, demonstrating an order of magnitude less for the ICP-MS. The 0.1 µg/L LOD is confirmed in Préndez et al., 2003 study for Antarctic peninsula lagoon water.

Trujillo et al., 2012 proposed a solid phase extraction method in conjunction with ICP-MS for the determination of trace metals in seawater (including zinc). The detection limit of the developed technique is proven to be equal to 0.26 µg/L for Zn.

2.2.2 Voltammetry

Voltammetry is one of the electrolytic analysis techniques, based on the discharge (oxidation or reduction) of an electroactive analyte. The analytic solution is introduced in the voltammetric cell, where three electrodes are present: working electrode, reference electrode and auxiliary or counter electrode, to close the circuit. Voltammetry is based on the electric signal (the current, i) provided by the analytical solution when a potential is applied to the working electrode. The applied potential can be variated so that the discharge potentials of the electroactive species in solution can be reached determining a variation of the resulting current.

2.2.2.1 Stripping Voltammetry

A particular application of voltammetry is stripping analysis, with which very low concentrations of analytes can be detected (sub nanograms).

Stripping analysis involves the concentration of the analyte into or onto the working electrode surface (Farghaly et al., 2014). This preconcentration step is followed by electrochemical measurements of the material stripped from the electrode. The accumulation phase that generates the analyte build-up is the reason of the major sensitivity of stripping voltammetry compared to direct voltammetry techniques.

Several stripping techniques have been proposed in time, in which element accumulation can be obtained using anodic/cathodic – ASV/CSV – or adsorptive processes, AdSV.

ASV and CSV can be considered as mirror processes. Anodic stripping voltammetry involves the analyte preconcentration onto the electrode by reduction, forming an amalgam at the cathodic potential; in the following phase, the amalgamated analyte is re-oxidized and stripped out the electrode applying an anodic potential. Cathodic stripping voltammetry involves the opposite process: positive deposition of the analyte when anodic potential is applied to the electrode and stripping of the element as a result of cathodic potential.

Adsorptive stripping voltammetry is quite similar to ASV/CSV techniques, with the difference in the preconcentration process, that is adsorption in this case. For metal ion detection, complexation reactions with ligand agents in solution precede the adsorption on the electrode surface.

The direct voltammetric determination of aluminium ion (Al^{3+}) in water appears to be difficult because of its negative reduction potential (-1.75 vs SCE), which is very close to that of other commonly present cations (sodium, barium and potassium, for example) (Chow et al., 2003). CSV with adsorption preconcentration phase gives successful results in aluminium detection in natural waters. A ligand is used to complex aluminium; the aluminium-ligand complex coats the electrode surface before being stripped under CSV action. A series of chemicals have been used as a ligand for CSV aluminium analysis. To give some examples, Pyrocatechol Violet is used in (Vukomanovic et al., 1991). Arancibia and Munoz., 2007 defined a cathodic adsorptive voltammetry with pyrogallol red ligand in the presence of a quaternary salt. LOD varies between 0.1 µg/L and 1 µg/L in these two applications.

ASV method is mainly used for zinc detection, as shown in (Ruecha et al., 2015) and (Kefala et al., 2003). An example of adsorption stripping voltammetry in zinc determination is given for seawater by (Arancibia et al., 2010) providing a low detection limit (0.05 µg/L for a short preconcentration time of 10 s).

2.2.3 UV-vis spectrophotometry

Spectrophotometry, as an optical method, is based on the light-matter interaction or in other words on the energy exchange between radiant energy and matter. UV-vis spectrophotometry is a particular application of absorption spectroscopy, which concerns the absorption of monochromatic light radiations of the visible (350 – 700 nm) and near UV (200 – 350 nm) fields. These radiations, when absorbed, cause molecular electronic transitions, detected as spectra. By generating a beam of radiation at a sample, the intensity of the radiation that passes through is detected. The transmitted energy can be used to calculate absorption. The absorbance is defined as:

$$A = -\log T = \log \frac{I_0}{I} \tag{2.26}$$

Where: T is the transmittance; I_0 is the intensity of the incident light; I is the transmitted intensity ($I<I_0$ due to light absorption by the solution).

Absorption is responsible for the attenuation of the incident radiation. The attenuation is specific to the hit sample, which has a characteristic absorbance spectrum. This allows discerning between different compounds (qualitative analysis). From a quantitative point of view, the amount of attenuation is considered, whereas it depends on the amount of substance, hence on the concentration.

The Lambert-Beer law relates the sample absorbance with the concentration of analyte in the same sample in a linear way:

$$A = \varepsilon \cdot b \cdot C \tag{2.27}$$

Where: ε (-) is the molar attenuation coefficient or absorptivity of the attenuating species; b (L) is the optical path; C (M L^{-3}) is the concentration of the attenuating species in the sample.

Absorption measurements of UV-vis light may be used to selectively determine metal ions, after the formation of metal-ligand complexes (Tria et al., 2007). This method has the advantage of being low-cost and fast, maintaining sensitivity and selectivity comparable with more sophisticated analytical approaches. Few chemical agents are also required, resulting in a higher safety profile for the use by non-expert operators.

A wide range of UV-vis spectrophotometric applications are reported in the literature for Aluminium detection. As ligand agents, aluminon and 8-hydroxyquinoline were traditionally employed. These two compounds exhibit high selectivity for aluminium even though they are not sensitive enough for low concentrations (Korenaga et al., 1980). Quercetin – an organic compound of flavonoids – is an example of reactant most recently used. In Lian et al., 2004 the aluminium chelating action of quercetin was exploited in a spectrophotometric method preceded by a RP-HPLC separation (LOD of $5 \cdot 10^{-8}$ mol/L and precision equal to 1.0% at the $5 \cdot 10^{-6}$ mol/L level). Pyrocatechol violet is often presented as an effective complexing agent. However, in real conditions, its action may be affected by the presence of other elements, such as fluoride and iron. Magnesium ions and phenanthroline avoid this kind of interference.

Zinc UV-vis spectrophotometric detection is a more recent practice. In the last twenty years, a series of colour-forming reagents for different samples' nature has been adopted. In water environment, Zincon is largely employed obtaining detection limits in the hundreds of nmol/L (LOD = 210 nmol/L in Säbel et al., 2010).

In this thesis work, simplified conditions were recreated: no real water samples were employed, but metals solutions prepared in deionized water by dissolving Zn^{2+} and Al^{3+} salts at mM concentrations. Subsequently, there were no species interfering with the selective complexation of the target compounds. Pyrocatechol violet and zinc complexations have been carried out for the direct determination of the selected elements, with no preconcentration phases needed and without the adding of other chemical agents.

3 Materials and methods

In order to evaluate zinc and aluminium behaviour, a series of laboratory tests were performed in saturated and unsaturated conditions. Column tests on sand have been used to study transport and propagation aspects; tracer tests preceded the metals injection phase to assess the behaviour of a non-reactive solute, as reference. Column tests gave as output breakthrough curves (BTCs), later modelled using the software HYDRUS 1D to estimate soil-water characteristic parameters: dispersivity and porosity retrieved from tracer tests, k_d (and R) from metal transport tests.

The mobility of a substance in the environment is controlled, among other processes, by adsorption (and desorption) mechanisms on a solid phase. Batch tests have been performed to understand metals' sorption equilibrium on standard soil. Sorption isotherms are the output of these studies, from which sorption isotherm coefficients have been determined. The k_d and R parameters retrieved from these studies was used to program column tests on standard soil.

Concentrations have been determined by spectrophotometric absorbance measurements. A UV-vis spectrophotometer (Specord S600, Analytik Jena, Germany) has been used throughout the procedure. This device was set to register absorbance values of each solution at its characteristic wavelength. The absorbance-concentration relation (calibration curves) outlined for each solution was used to derive information about concentration.

The investigated metal solutions (Zn and Al in the form of chlorides) exhibit a natural peak in UV region – around 200 nm – like all the salts. For more accurate and specific detection, colorimetric methods have been developed. Using the UV-vis spectrophotometry techniques, the recorded absorbances in the visible spectrum were those of the two metal-ligand complexes.

3.1 Calibration curves

Concentration values can be directly derived from absorbance measurements in the case of a linear relationship between absorbance and concentration, as expressed by the Lambert-Beer law. The curve that, in the field of chemical analysis, describes the linear relationship between absorbance and concentration is called calibration curve. It is a regression model that allows predicting the unknown concentration of the analytes of interest starting from measurements of known concentrations. To have a robust calibration curve, the absorbance measurements of a series of samples (at least 6), well distributed in the range of concentration of interest, are recommended. The linear interpolation of such concentration-absorbance points is the resulting calibration curve. In this study, each prepared solution needed the realization of a specific calibration curve. In this section, the calibration method for all the metal solutions is described, apart from metal complexes, which is discussed in the 3.2 paragraph along with the detailed description of the analytical method developed on purpose in this thesis.

Metals solution

Stock solution for calibration: 100 mM $ZnCl_2$ and $AlCl_3$ solutions.

Working solutions: various volumes of 100 mM $ZnCl_2$ and $AlCl_3$ solutions, prepared by proper dilution with DIW. The concentration of the working solutions corresponded to 75, 50, 35, 25, 10, 5 mM of the two different compounds.

The full absorbance spectrum of each sample has been recorded (Figure 3.1 and Figure 3.2).

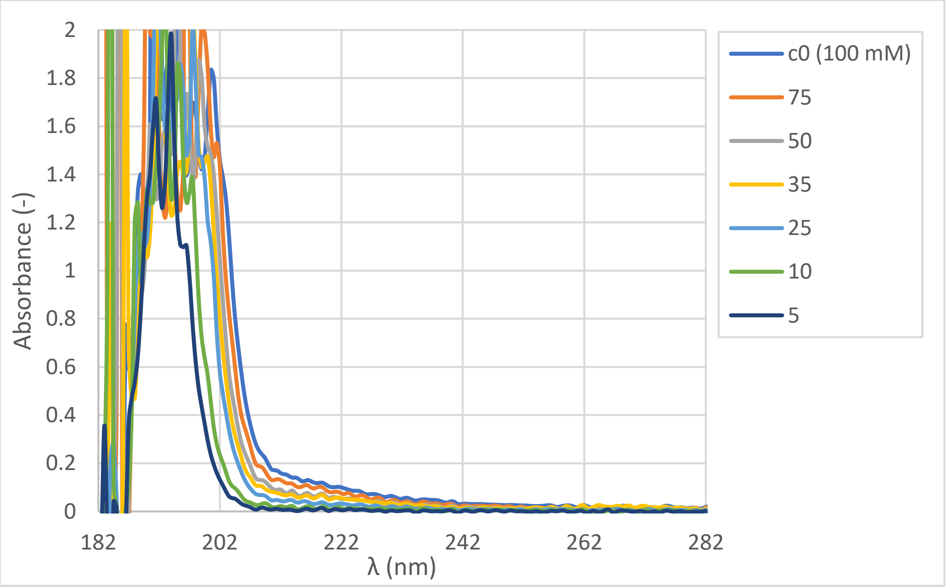

Figure 3.1 - $ZnCl_2$ spectrum

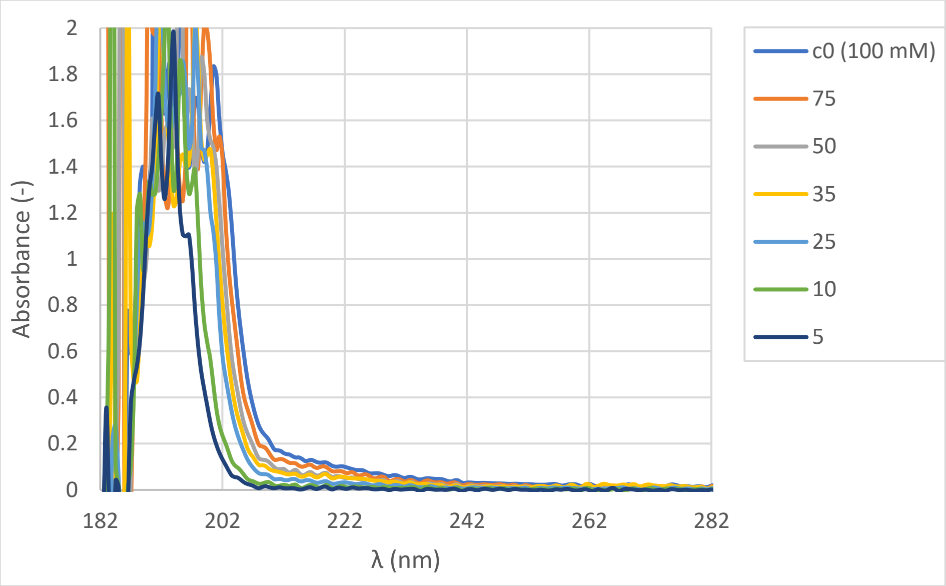

Figure 3.2 - $AlCl_3$ spectrum

In correspondence to the wavelength that shows a clear linear correlation between absorbance and concentration, the calibration curve is drawn. In Figure 3.3 the calibration curve for $ZnCl_2$ at 198.5 nm is reported, limiting the interpolation to less concentrated samples (concentrations closer to the values used in the study). In Figure 3.4 the calibration curve retrieved for $AlCl_3$ compound at 203 nm is shown.

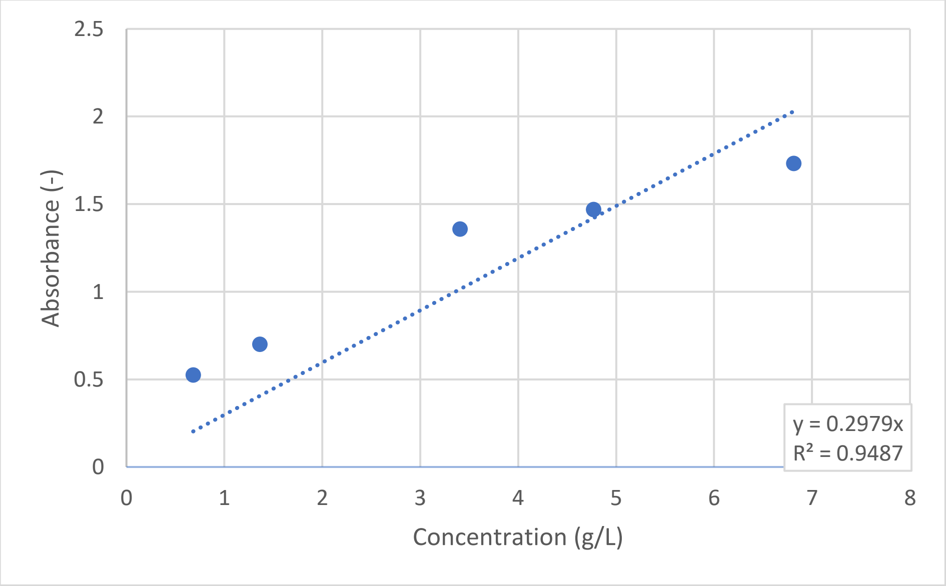

Figure 3.3 - $ZnCl_2$ calibration curve

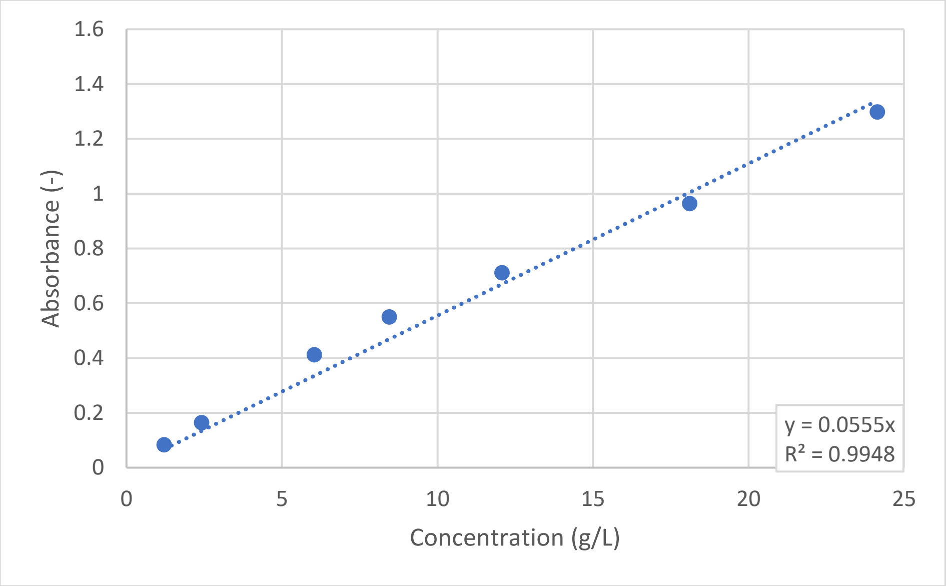

Figure 3.4 - $AlCl_3$ calibration curve

3.2 Metals detection

3.2.1 Zinc

The method proposed by (Abdulla, 2016) was used as the basis to develop a Zinc spectrophotometric detection protocol in the specific operative conditions of this work. The method is based on the Zn^{2+} - Zincon complexation reaction.

Zincon – short name for 2-carboxy-2'-hydroxy-5'-sulfoformazylbenzene – when not in solution appears as a dark reddish-purple powder. It is an analytical reagent for a long time used for Zn detection. As early as 1954, Rusch and Yoe showed the potentiality of Zincon to simultaneously determine zinc and copper ions in aqueous solutions. Figure 3.5 and Figure 3.6 show the Zincon structure and the formed metal-Zincon complex, respectively.

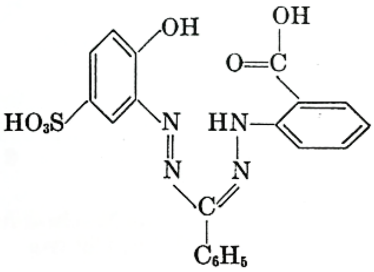

Figure 3.5 - Zincon structure

The reaction in one-to-one Zn^{2+}-Zincon ratio in a specific pH range (around 9 – 10) returns a blue coloured complex, that exhibits the maximum absorbance at ≈ 620 nm. However, considering the complex stoichiometry (Abdulla, 2016),

$$\frac{[Zn^{2+}]}{[Zincon]} = \frac{1}{2}$$

the defined procedure works in Zincon excess to be sure that the metal-ligand bond did not reach saturation. The absorbance values were recorded at 620 nm. At this wavelength, the spectrum (Figure__) doesn't exhibit the absolute peak, observed around 495 nm, but there is good linearity in the retrieved calibration curve.

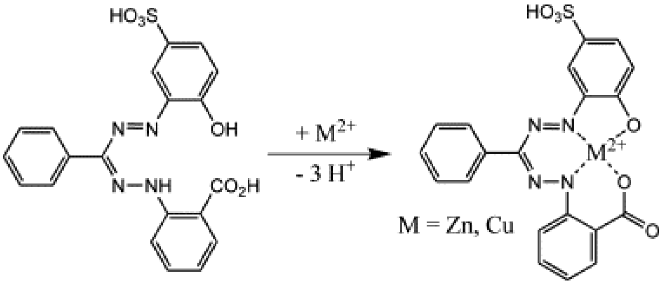

Figure 3.6 - Structures of Zincon (2-carboxy-20-hydroxy-50-sulfoformazylbenzene) in its metal-bound forms (from Säbel et al., 2010)

3.2.1.1 Calibration curve

Chemical reagents and solution

Zincon stock solution: 1 mM Zincon solution. 2.4 mg Zincon (MW 480.43g/mol) were dissolved in 1 ml NaOH 1M prior dilution to 50 mL with DIW.

Zn^{2+} stock solution: 1 mM $ZnCl_2$ solution. 6.8 mg $ZnCl_2$ were dissolved in 50 ml DIW.

Zn^{2+} working solution: various volumes of 1 mM $ZnCl_2$ solution.

Solutions preparation: in 10 mL plastic volumetric flasks, 1 mL of 1 mM Zincon solution was introduced with various volumes of 1 mM $ZnCl_2$ solution. DIW is used to make up to the mark.

The selected volumes of $ZnCl_2$ solution correspond to: 1, 0.75, 0.5, 0.375, 0.25, 0.075, 0.05 mL, from the most concentrated to the least concentrated Zn^{2+} sample. Figure 3.7 shows the spectrum that each solution exhibits.

The calibration curve drawn between absorbance and Zn^{2+} concentration indicates that the metal can be effectively determined between $5 \cdot 10^{-5}$ and $1.25 \cdot 10^{-6}$ M (Figure 3.8).

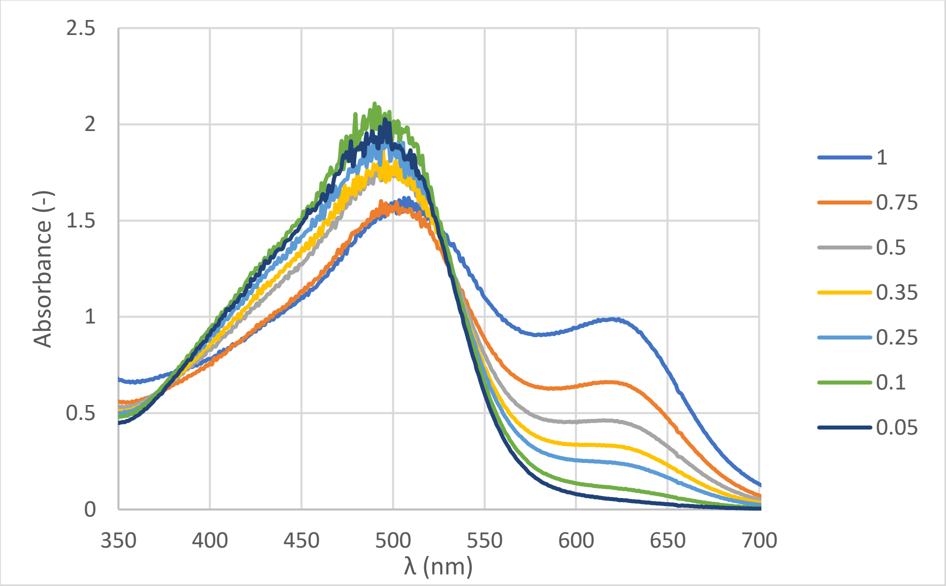

Figure 3.7- Zn2+- Zincon solutions spectra

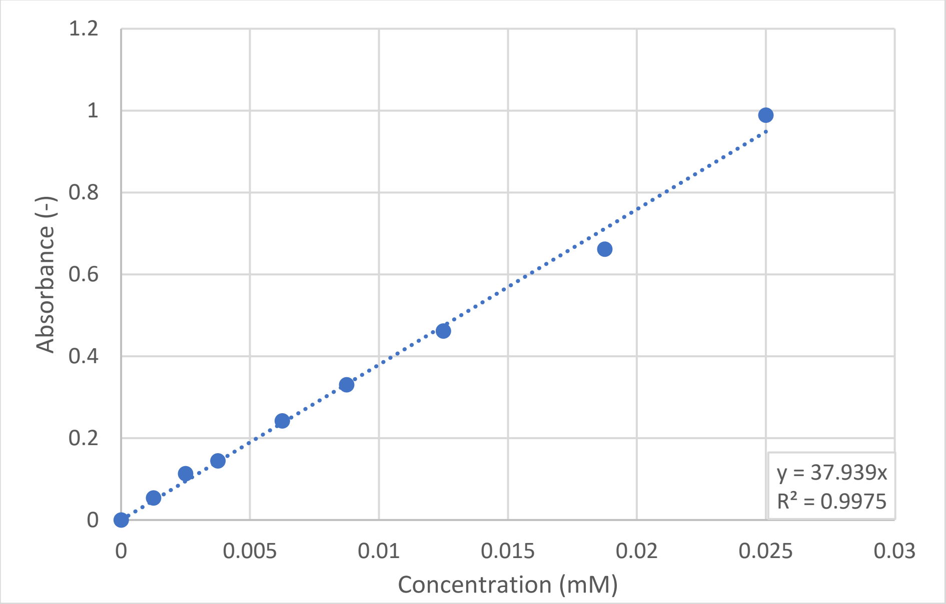

Figure 3.8- Zn2+ - Zincon calibration curve

3.2.2 Aluminium

MiPAF, 2001 spectrophotometric method for aluminium detection has been used to develop a more suitable solution for the specific case. The ligand agent is Pyrocatechol Violet (3,3',4'-

trihydroxyfuchsone-2"-sulphonic acid) that forms a blue complex with aluminium in optimal conditions (pH around 6.1 – 6.2). When not in solution it is a reddish-brown crystalline powder. Figure _ shows its molecular structure.

3.2.1.1 Calibration curve

Chemical reagents and solutions

Pyrocatechol violet stock solution: 1 mM PCV solution. 75 mg PCV (MW 386.38 g/mol) were dissolved in 20 mL DIW prior dilution to 200 mL with DIW.

Potassium acetate solution: 0.4 M CH_3COOK solution. 3.9 g Potassium acetate (98.15 g/mol) were dissolved in 100 mL DIW.

Ascorbic acid solution: 0.4 M $C_6H_8O_6$ solution. 7 g Ascorbic acid (MW 176.12 g/mol) were dissolved in 100 mL DIW.

Al^{2+} stock solution: 1 mM $AlCl_3$ solution. 12 mg $AlCl_3$ were dissolved in 50 ml DIW.

Al^{2+} working solution: various volumes of 1 mM $AlCl_3$ solution.

Before the calibration phase, the optimal volumes of the reagents in solution were determined. The absorbance variation in time was evaluated for different ascorbic acid/potassium acetate ratios for a one-to-one Aluminium-PCV relationship (0.5 mL each in a 10 mL flask):

- No ascorbic acid
- Ascorbic acid/potassium acetate 1:4
- Ascorbic acid/potassium acetate 1:6
- Ascorbic acid/potassium acetate 1:10

Potassium acetate volume was kept constantly equal to 1 mL.

Absorbance values were recorded for about an hour. The peak oscillation, small in all cases, were lower in the no ascorbic acid-containing solution (Figure 3.10). Thus, calibration operations were made for different dilutions of aluminium having in solution only potassium acetate and PCV reagent.

Solutions preparation: in 10 mL plastic volumetric flasks, 0.5 mL of 1 mM PCV solution and 1 mL 0.4 M potassium acetate was introduced with various volumes of 1 mM $AlCl_3$ solution. DIW is used to make up to the mark.

The selected volumes of $AlCl_3$ solution correspond to: 1, 0.75, 0.5, 0.375, 0.25, 0.075, 0.05 mL, from the most concentrated to the least concentrated Al^{3+} sample. Figure 3.11 shows the spectrum that each solution exhibits.

The calibration curve drawn between absorbance and Al^{2+} concentration indicates that the metal can be effectively determined between $2.5 \cdot 10^{-5}$ and $2.5 \cdot 10^{-6}$ M (Figure 3.12).

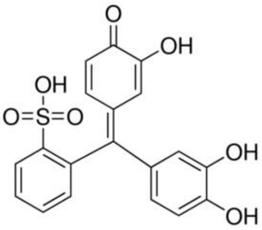

Figure 3.9 - Pyrocatechol Violet structure

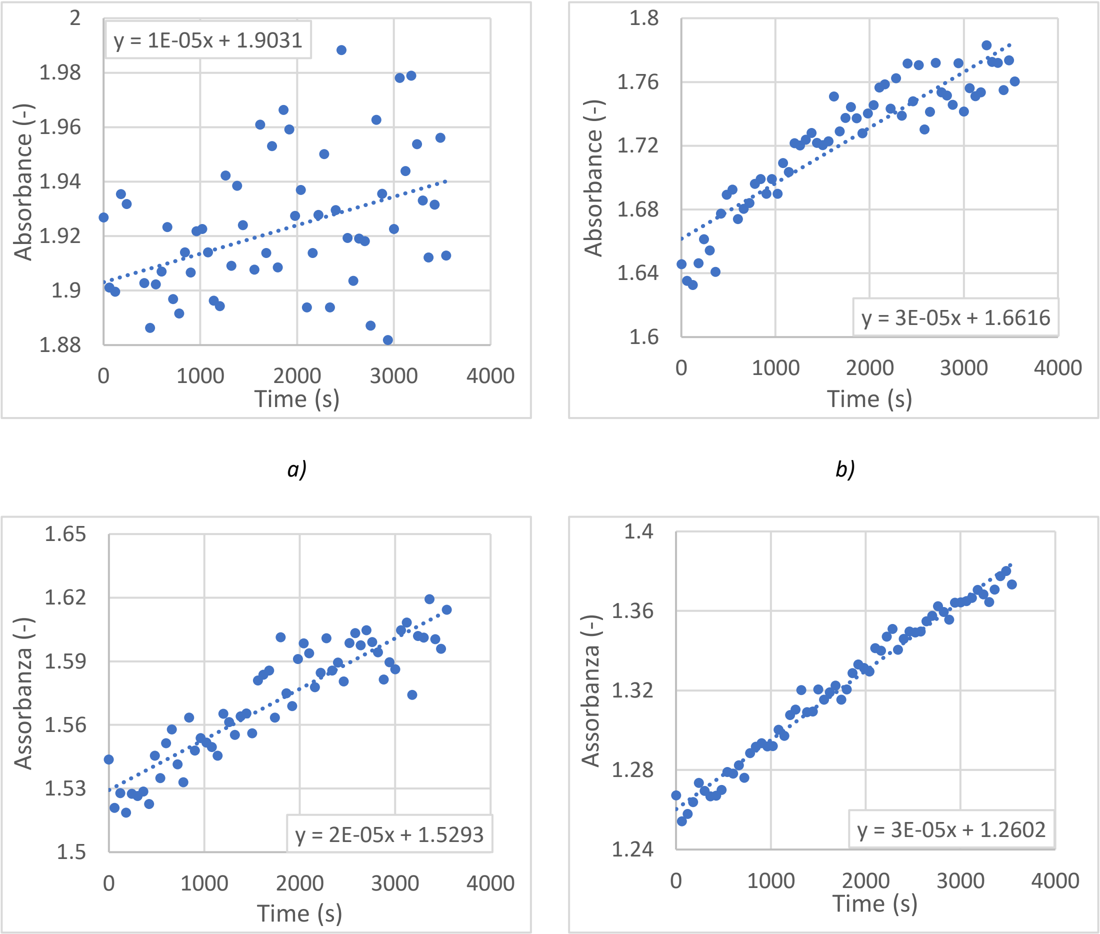

a)

b)

c)

d)

Figure 3.10 - Variations in the absorbance peak of for solutions with different potassium acetate/ascorbic acid ratio. a) no a) no ascorbic acid; b) 1:4 ratio ascorbic acid/potassium acetate; c) 1:6 ratio ascorbic acid/potassium acetate; d) 1:10 ratio ascorbic acid/potassium acetate.

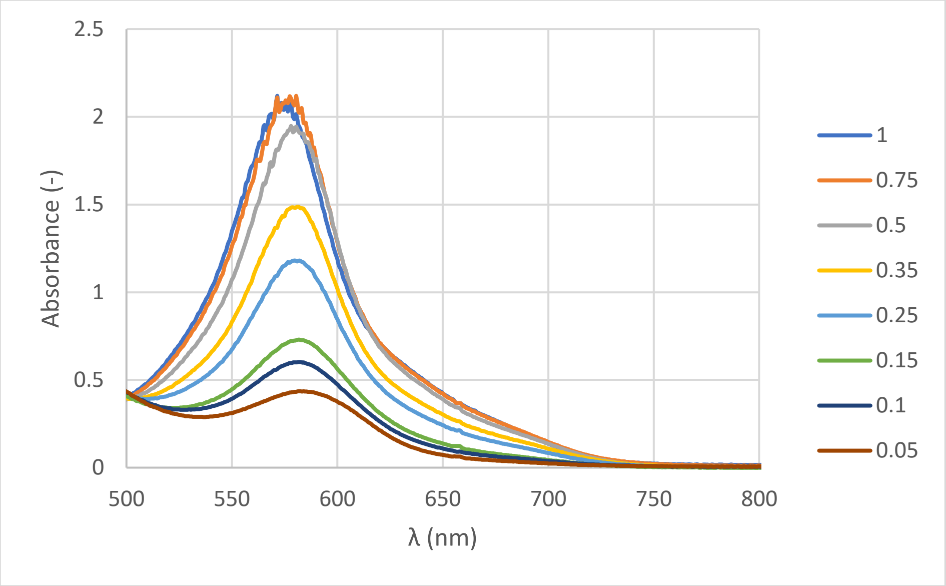

Figure 3.3 – Al3+ – PCV solutions spectra

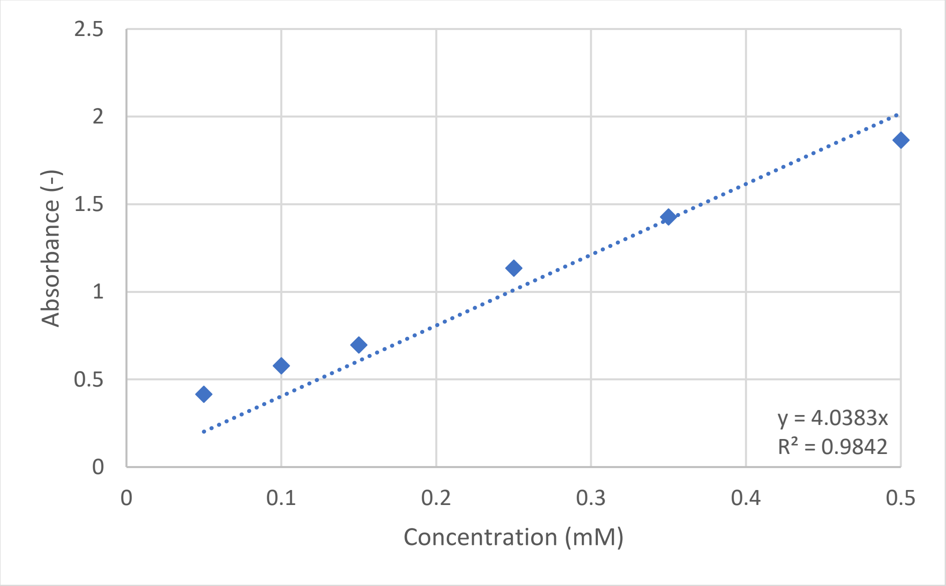

Figure 3.4 – Al^{3+} – PCV calibration curve at 573.5 nm

3.6 Batch tests

A set of batch experiments was conducted to study the equilibrium sorptive behaviour of the two studied metals on LUFA standard soil n. 22 (Soil chemical and physical characteristics according to Good Laboratory Practice are reported in Appendix).

The batch investigations were intended to determine the sorption parameters for the selected solid phase according to the outlined sorption isotherms. A sorption isotherm relates the adsorbed metal mass per unit mass of the solid phase with the equilibrium solute concentration into the solution. The influence of temperature and pH on sorption mechanisms is very strong, hence the need to keep temperature – and pH – constant during the tests.

Seven samples were prepared: 2 g of soil were introduced in five 50 mL flasks, into which the contaminant solutions at the different $ZnCl_2$ and $AlCl_3$ concentrations (10 – 7.5 – 5 – 3.5 – 2.5 – 1 – 0.75 mM) were added. 1 mL from each contaminant solution was taken for blank analysis. The flasks were mixed vigorously at ambient temperature for almost 24 h to ensure that the equilibrium was reached. A 20 min centrifugation allowed the soil-liquid phase separation, and the aqueous phase was analysed using the previously described detection protocols (Paragraph 3.2). In Figure 3.13 is schematized the overall process.

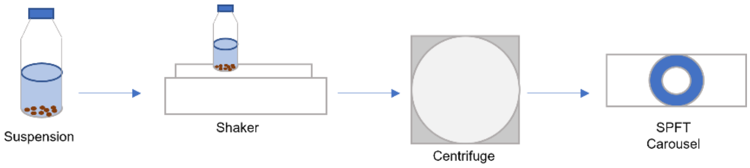

Figure 3.5- Bach test process

The amount of the test substance adsorbed on the soil sample is calculated with the indirect method, as the difference between the metal amount initially present in the solution – retrieved from blank analysis – and the amount at the end of the experiment. Considering the volume of the solution and the mass of the adsorbent material, the relation can be expressed as follows:

$$q_e = \frac{(C_0 - C_e) \cdot V}{m} \tag{3.2}$$

Where: q_e is expressed as mg_{solute}/g_{soil}; C_0 and Ce (mg/L) are respectively the initial and equilibrium metal concentration; V (L) is the volume of the aqueous solution; m (M) is the mass of the soil phase.

The three most commonly observed sorption models have been used to analyse the sorption isotherms: linear, Freundlich and Langmuir models. For particular data distributions, other options have been considered. The optimum sorption process was determined according to R^2 values, obtained for interpolation of sorption values.

The sorption behaviour in its general form can be described by the equation:

$$S = \frac{K_d C^{\beta}}{1 + \eta C^{\beta}} \tag{3.3}$$

Where: S is the concentration of zinc adsorbed into the solid phase at equilibrium (mg g–1); C is the liquid phase resident concentration of zinc at equilibrium (mg L^{-1}), and K_d, β and η are the soil–water distribution coefficient, the Freundlich exponent and the Langmuir coefficient, respectively. When β=1, Eq. 3.3 becomes a Langmuir isotherm; when η=0, the equation becomes a Freundlich isotherm and when both β=1 and η=0, it leads to a linear adsorption isotherm.

3.2 Sand-packed column tests

Column tests set-up (Figure 3.14) consisted of a plastic tube with 1.6 cm inner diameter mounted on a support to establish the desired vertical flow. The tube was filled with 55 g of pre-washed silica sand (DORSILIT n. 7, Dorfner, Germany, whose characteristics are reported in Appendix) introduced in layers by adding and gently tapping small amounts of sand-deionized water suspension. The final result was a 17 ± 0.3 cm sand-packed column. Two plastic plugs at both ends fixed the sand in place. The feed downflow rate was supplied and maintained throughout the test using of a peristaltic pump. By means of a pipe, the column effluent passed through a flow cell in the spectrophotometer carousel for absorbance measurements. From the injection tank (solution at the initial concentration) a pipe ran to another flow cell in the spectrophotometer carousel for the initial absorbance (A_0) measurement. The spectrophotometer was set to perform measurements with a 60-second frequency.

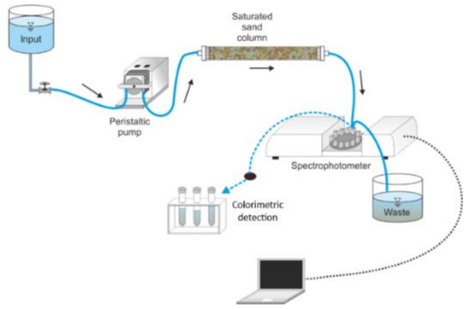

Figure 3.14- Sand column set up. In the figure, an indication of the metals colorimetric detection performed in parallel with the on-line spectrophotometric measures is reported

All the column experiments (tracer tests, Zn and Al injections) were performed injecting a constant flow rate of $1.67 \cdot 10^{-8}$ m^3/s. Before and after the solute injection, pre-flushing and post-flushing phases were done. A schematic indication of the duration of each phase, expressed in PV, is reported below.

For saturated tests:

- Pre-flushing with DIW: ≈ 3 PV
- Solute injection: ≈ 4 PV
- Flushing with DIW: ≈ 3 PV

For unsaturated tests:

- Pre-flushing with DIW: ≈ 2 PV
- Solute injection: ≈ 3 PV
- Flushing with DIW: ≈ 2 PV

The PV (Pore Volume) parameter, determined by tracer tests, is a time, measured in correspondence to an output concentration of dye equal to half C_0.

3.2.1 Saturated conditions

The sand accurately washed to eliminate colloids and impurities (following a specific procedure consisting of in ≈12 h NaOH 100 mM, washing followed by 3 tap water washing and 3 DIW washing), has been introduced in layers by adding small amounts of a sand-deionized water suspension to avoid air bubbles in. During packing, up-flow of DIW has always been guaranteed to prevent accidental desaturation by gravity. Two filters at the top and at the bottom of the sand column prevented sand particles from infiltrate and clog both the inlet and outlet tubes. The influent and the effluent solutions were continuously measured by the UV-vis spectrophotometer. The extracted data led to BTCs construction.

3.1.1 Tracer tests

Once verified no air entered during the packing procedure, the tracer test started. The feed consisted of 20 g/L Bromophenol Blue (BFB) solution. BFB, being a dye, makes visual and quantitative detection easy. The absorbance of the solution has been measured at 598 nm, where the BFB absorbance spectrum showed the peak. The injection has been carried on since absorbance signals over time reached a plateau. Then DIW was flushed until zero concentration of the tracer solution was detected.

3.1.2 *Metals injection*

After the tracer injection and a post-flushing, aimed at completely remove eventual tracer residuals, metals injection experiments were conducted, separately for zinc and aluminium. For zinc transport tests, the influent consisted of a $ZnCl_2$ 10 mM solution, while for aluminium $AlCl_3$ 10 mM solution was injected. From calibration tests, the two solutions exhibit good concentration-absorbance linearity at 198.5 nm and 203 nm. As for tracing tests, metal transport tests were monitored continuously by the UV-vis spectrophotometer.

Meanwhile, spot samplings (25 µL samples) of the column outlet were performed at fixed frequencies: two minutes in the test phase between the start of injection and the first increase in absorbance, thus concentration; one minute in the ascending branch of the absorbance-time curve recorded by the spectrophotometer and the same in the descending branch. The collected material underwent the defined metals' detection procedures. A BTC curve was reconstructed. This phase was useful for validating the method.

3.2.2 Unsaturated conditions

On the same column on which saturated tests were performed, tests in unsaturated conditions were established. Unsaturated columns were obtained after drainage by gravity. The pump was switched off, the inlet and outlet tubes were disconnected, and the column was let drip. The released water was collected and weighted, obtaining a measure of the gravitational water, thus of the effective porosity. Once desaturation was completed, the constant flow rate was re-established, by turning on the pump and reconnecting the inlet tube. From this moment (t_1), the time t_2 that water takes to exit again the column has been measured. All these led to determine the unsaturated water content (θ_{unsat}), as sum of the water content after desaturation (θ_d) and the injected water before the flux was restored (θ_{inj}), as shown by the formula:

$$\theta_{unsat} = \theta_d + \theta_{inj} = \frac{\left(nV - \frac{m}{\rho_w}\right)}{V} + \frac{Q \cdot (t_1 - t_2)}{V} \tag{3.1}$$

Where: n (-) is the porosity of the sand column; V (L^3) is the volume of the sand column; m (M) is the mass of the drained water; ρ_w (M/L^3) is the water density; Q (L^3/T) is the discharge rate; t_1 and t_2 (T) are the two times mentioned above.

This parameter is essential for the further HYDRUS-1D modelling phases.

For metals injection, in parallel with spectrophotometric continuous measurements, punctual sampling with subsequent metals detection by complexation were performed, as done for saturated conditions.

3.3 Soil-packed column tests

Unsaturated tests were run on soil columns. LUFA standard soil (n. 2.2) was employed .35 g of soil were introduced in the plastic tube, giving a 15 ± 0.3 cm soil-packed column. As a first step, the column was fully saturated with deionized water. The solution was injected from the bottom of the column at a slow rate to prevent the formation of preferential flow pathways. The following desaturation phase was obtained by removing the DIW feed and letting the column drip.

Figure 3.15- Soil-column metal injection tests set-up

After the tracer test, two in-parallel metal injection tests were run, for zinc and aluminium, separately. Spectrophotometer continuous measurements were proven to be useless in these specific experiments: the massive presence of other salt species and impurities affects the absorbance reading around 200 nm. Manual punctual sampling was performed in order to derive the BTCs. The overall experimental set-up, similar to those of sand-packed column tests, is reported in Figure 3.15.

Due to the retardation factor estimated high from batch tests, the experiments were performed in a long time (24 h). For this reason, a fraction collector was installed to take samples at a fixed frequency (25 minutes). The following detection operations with complexation were conducted on 25 µL solution.

3.4 Simulation of zinc release from mining waste

Once the overall behaviour of the contaminants in the unsaturated zone was known, the work focused on the simulation of a real scenario. The release of materials resulting from mining activities has been represented. It is interesting to see the potential environmental impact of an accidental soil discharge and understand how well the soil can perform as a filter/barrier for the groundwater system.

A pulse injection test has been conducted with zinc enriched material. It was a rougher concentrate obtained from the first stage of froth flotation on Gorno mining activities waste, characterized by the presence of 89% sphalerite, a Zn^{2+} bearing mineral (information about the composition and XRD images are reported in Appendix). Batch tests have guided the definition of the optimal mass to use and pH conditions to establish for the column test. 2, 1 and 0.5 g of the material were placed in 50 mL flasks. Three environments at different pH have been analysed by varying the solution: DIW, DIW + various volumes of citric acid (pH ≈ 4.5), and pH 3.6 citric acid-trisodium citrate buffer. The situation that provides for better zinc release was with 2 g rougher material in the pH 3.6 solution. Therefore, a mixture of 4 g rougher material and 15 mL pH 3.6 buffer solution was prepared for the following injection.

The test was carried out on a sand-packed column previously unsaturated by gravity in four consecutive steps, as follows:

- Pre-flushing with pH 3.6 buffer solution for ≈ 6 PV to conditionate the column;
- Pre-flushing with DIW for ≈ 2 PV;
- Pulse injection of the rougher- buffer solution mixture;
- Flushing with DIW for ≈ 2 PV.

After the pulse injection, samples from the bottom of the column were collected at a fixed frequency (30 s) until the end of the dripping. Then, during the flushing with DIW, the sampling operations happened every 2 minutes. 25 µL were subject to the detection phase with complexation. The obtained data were processed giving the characteristic path in a time-mass graph.

3.6 Data modelling

The breakthrough curves (BTCs) obtained from column tests were modelled using HYDRUS-1D, open-source software to simulate the one-dimensional movement of water, heat and solutes in variably saturated conditions (Šimůnek et al., 2013). This modelling phase, together with the experimental data fitting, allows to derive water flow and transport parameters characteristic of the test type, tracer or metal injection, in saturated or unsaturated conditions, as summarized:

- Saturated tracer tests: saturated soil water content, θ_s (-) and longitudinal dispersivity, α_L (L);
- Saturated metal injection tests: adsorption isotherm coefficient, K_d (M^{-1} L^3);
- Unsaturated tracer tests: volumetric water content θ (-), saturated hydraulic conductivity K_s (L T^{-1}), hydraulic conductivity K (L T^{-1}) and longitudinal dispersivity, α_L (L);
- Unsaturated metal injection tests: adsorption isotherm coefficient, K_d (M^{-1} L^3).

The K_d parameter, estimated from injection tests modelling, is then used to derive the retardation factor, R, according to the 2.15 equation.

The HYDRUS-1D package numerically solves the Richards equation (2.21) for variably saturated water flow in order to determine θ, θ_s and K parameters.

$\theta(h)$ and K(h) soil hydraulic properties in variably saturated conditions are in general non-linear functions of the hydraulic pressure head. HYDRUS-1D software implements five analytical models for their estimation: Brooks and Corey; van Genuchten; Vogel and Císlerová; Kosugi and Durner. The Van Genuchthen model was adopted for this work.

The advection-dispersion equation below, is used to describe solute transport:

$$\frac{\partial \theta C}{\partial t} = \frac{\partial}{\partial x}\left(\theta D \frac{\partial C}{\partial x}\right) - \frac{\partial qC}{\partial x} \tag{3.4}$$

Where: D ($L^2 T^{-1}$) is the hydrodynamic dispersion; q ($L T^{-1}$) is the water flux.

The dispersion coefficient is given by the equation:

$$\theta D = D_L |q| + \theta D_w \tau_w \tag{3.5}$$

Where: D_w ($L^2 T^{-1}$) is the molecular diffusion coefficient in free water; τ_w (-) is the tortuosity factor in the liquid phase.

In this work, the tortuosity factor is considered and determined according to Millington and Quirk, 1961 relation:

$$\tau_w = \frac{\theta^{7/3}}{\theta_s^2} \tag{3.6}$$

This tortuosity model, being derived assuming randomly distributed particles of equal size, for sands is in fact expected to perform better than Moldrup one, which is better suited for soils (Simunek et al., 2013).

3.6.1 Chemical non-equilibrium

To better simulate the metals transport through porous media, a chemical non-equilibrium model (CNEM) was implemented. The CNEM corresponds to a kinetic behaviour because the adsorption process takes time to reach equilibrium between the concentration in the liquid and the solid phase (S. Jellali et al., 2010). Non-equilibrium transport occurs because the interaction sorbate-sorbent is slow in comparison to the residence time in column. In other words, more time is request to the sorbate to reach the equilibrium.

According to Simunek et al., 2013, in such cases, the transport equation needs to be modified, including the description of the sorption process. If a first-order kinetic is assumed, it results:

$$\frac{\partial \theta C}{\partial t} + \rho \frac{\partial S^k}{\partial t} = \frac{\partial}{\partial x}\left(\theta D \frac{\partial C}{\partial x}\right) - \frac{\partial qC}{\partial x} - \phi \tag{3.7}$$

Assuming one-site sorption model, the adsorption in the generical form, is described as follows:

$$S_e = f_e \frac{k_d C^{\beta}}{1 + \eta C^{\beta}} \tag{3.8}$$

Where f_e (-) is the fraction of the sorption sites in equilibrium with the liquid phase, equal to zero for the selected nonequilibrium model and S_e ($M\,M^{-1}$) is the sorbed concentration at equilibrium.

It is also valid the equation below:

$$\frac{\partial S^k}{\partial t} = \omega \left(f_e \frac{k_d C^{\beta}}{1 + \eta C^{\beta}} - S_k \right) \tag{3.9}$$

Where ω (T^{-1}) is the first-order rate coefficient, S^k ($M\ M^{-1}$) is the sorbed concentration of the kinetic sorption sites.

3.6.2 Tracer tests modelling

3.6.2.1 Saturated conditions

The pre-processing phase involved inserting a series of parameters useful for the correct functioning of the software. These parameters are listed below:

- Geometry information:
    - column length, 17 ± 0.3 cm;

- Soil hydraulic parameters:
    - Saturated hydraulic conductivity K_s calculated from the Darcy's law (2.5), equal to $8.29 \cdot 10^{-5}$ m/s.
    - n, α set equal to 1 and 0 in saturated conditions, respectively.
    - Tortuosity parameter l, equal to 0.5, as suggested by Mualem, 1976.
    - Saturated water content θ_s, to be estimated.
- Water flow boundary conditions:

- upper BC: constant flux:

$$q(x = 0, t) = q$$

- lower BC: constant pressure head:

$$h(x = L, t) = \mathrm{L}$$

- IC: pressure head profile.

$$h(x, t) = x$$

Solute transport boundary conditions:

- upper BC: solute concentration during the injection:

$$\frac{C}{C_0}(x = 0, t) = 1 \qquad \text{For } 0 < t < t_{end}$$

$$\frac{C}{C_0}(x = 0, t) = 0 \qquad \text{For } t < tend \text{ and } t > t_{end}$$

- lower BC: zero concentration gradient

3.6.2.2 Unsaturated conditions

Unsaturated test modelling requires a more articulated procedure, consisting of three iterations. In the first step, the tests have been modelled as for saturated conditions. The volumetric soil water content is the result obtained from the inverse solution. The second and third steps lead to the estimation of the saturated hydraulic conductivity and dispersivity parameters.

α and n parameters acquire significance in the modelling of unsaturated conditions. They were set equal to 9.83 and 4.73, respectively. These values are obtained from the soil water retention curves retrieved for the used sand material.

For unsaturated tests in soil columns, in absence of study on soil-water retention curves, a and n values predicted by the software were used for sandy loamy soil, according to the granulometric fractions:

- 76% sand;
- 15% silt;
- 9% clay.

The result was:

- a = 3.74;
- n = 1.5186.

The boundary conditions this time were modified into:

- Upper BC: constant flux:

$$q(x = 0, t) = q$$

- Lower BC: water content from desaturation

$$\theta(x = L, t) = \theta_{unsat}$$

- IC: constant water content from desaturation

$$\theta(x, t = 0) = \theta_{unsat}$$

3.6.3 Metal injection modelling

For metal injection modelling, data obtained from tracer tests were used in order to determine the K_d parameters, thus retardation factor, R, according to Eq. 2.15. and Eq. 2.16. A linear one-site chemical non-equilibrium was used to consider a first-order decay of solutes.

4 Results and discussion

4.1 Batch tests

In this section, the results of batch tests are reported for both zinc and aluminium contaminants. For a more concise discussion, only the sorption isotherms with the best fit are shown: Langmuir (and IV type) isotherm for zinc, and linear isotherm for aluminium.

4.1.1 Zinc

For zinc contaminant, the batch test on standard soil allowed the reconstruction of the sorption isotherm in Figure 4.1. While the concentration at equilibrium decreases, the sorption capacity seems to reach a plateau, to line up for lower values, almost as the trend of a IV type sorption isotherm. This trend is not confirmed since it seems due to the last point only. Removing the last point from the analysis, the points are better described by a Langmuir isotherm (Figure 4.2). According to the R^2 (0.9737 vs 0.9422 Langmuir fits better than linear isotherm. This is confirmed by Behroozi et al., 2020, who verified the $ZnCl_2$ sorption capacity of natural soil at lower zinc concentrations ($ZnCl_2$ solutions from 100 mg/L to 10 mg/L) and observed a good fitting with the Langmuir model.

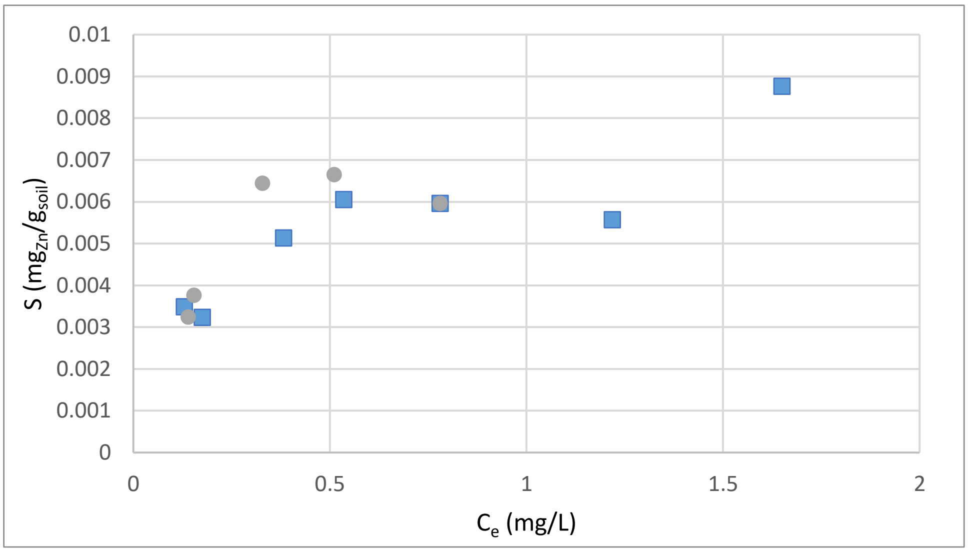

Figure 4.1 - IV type sorption isotherm for $ZnCl_2$

Langmuir isotherm, is expressed by the relation:

$$S = \frac{\alpha\beta C}{1 + \alpha C}$$

with the meaning of the α and β parameters explained in the literature background chapter (2.1.2.1 paragraph).

An estimate of the retardation factor, calculated through Eq. 2.16:

$$R = 1 + \frac{\rho_b}{\phi_e}\left(\frac{\alpha\beta}{(1+\alpha C)^2}\right)$$

for the injected concentration in the following column tests (10 mM) results equals to 1 with

- $\alpha = 6.82\ \mathrm{l/mg_{Zn}}$
- $\beta = 7.40 \cdot 10^{-3}\ \mathrm{mg_{Zn}/g_{soil}}$

The retardation factor found differs by one order of magnitude from that obtained from the soil column test (see paragraph 4.2).

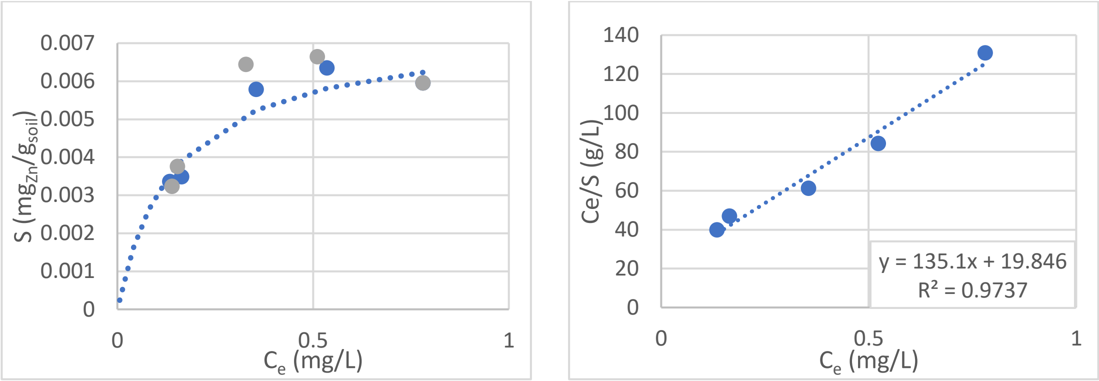

a)

b)

Figure 4.6- Langmuir isotherm for $ZnCl_2$ in the a) not-linearized form and b) linearized form

4.1.2 Aluminium

For $AlCl_3$ the data from batch tests are adequately interpolated by a linear function. According to the R^2 parameter (0.9449), the linear isotherm best describes the obtained data points. In Figure 4.3 the above-mentioned sorption isotherm is shown.

The linear sorption isotherm is defined by the following equation:

$$S = K_d \cdot C_e$$

K_d is the slope of the tendency line equation, thus it is equal to 0.0122 L/g. From this value, recalling the Eq. 2.15:

$$R = 1 + \frac{\rho_b}{\phi_e} K_d$$

R results equal to 76, higher than that obtained from the transport test in soil (see paragraph 4.2).

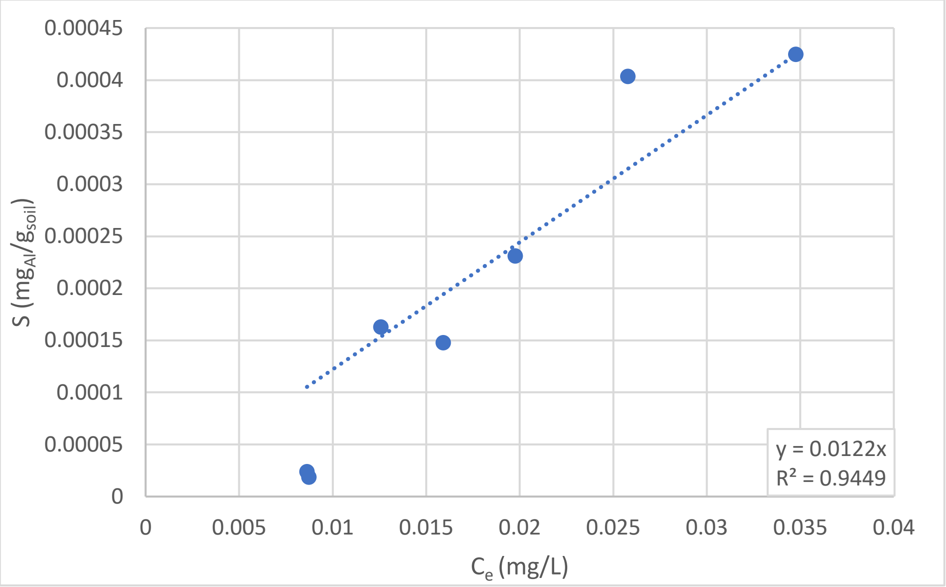

Figure 4.3 – $AlCl_3$ linear sorption isotherm

4.1 Sand-packed column tests

In this section, the results of the column tests on sand material are discussed. As already said, all the metals injection tests were preceded by tracking operation with bromophenol blue. The description is structured according to this framework, with an initial analysis of BTCs' dye, followed by a comparison with those of the metals. This qualitative comparison gave a measure of the peculiar behaviour of the two metals. The discussion starts from zinc, then moves to the aluminium study. In all the graphs the HYDRUS fitting is overlapped to the data obtained from the spectrophotometric readings. Metals modelling was done using the one-site CNEM, thus along with the K_d parameter, the mass transfer coefficients ω are listed.

4.1.3 Zinc

4.1.3.1 Saturated conditions

Bromophenol Blue BTC

In Figure 4.4 the result of the saturated tracer test is shown. The typical behaviour of a tracer is observed: a rapid increase in C/C_0 until the unit value is reached. Values slightly higher than 1 does not have any physical significance; they are probably linked to operative issues related to the flow cells employed.

The software provided for a good fitting of the experimental data, as demonstrated by the R^2 values, very close to 1 (Table 4.1), better in the sorption, than in the desorption phase of BTC.

Through tracer tests, the duration of the pore volume parameter is determined (Table 4.1). In the same table, the water content is reported, together with the hydraulic conductivity and dispersivity. The very low α_L value suggests a homogeneous packing of the sand since a relation between the dispersivity in the flow direction and the mean grain size diameter exists at laboratory scale (Jellali et al., 2003).

Table 4.1- Transport parameters obtained from BFB tracer test in saturated conditions (Zn injection column)

PV (min)	θ_s (-)	α_L (m)	R^2 (-)
13.23	0.395	$1.39 \cdot 10^{-3}$	0.99892

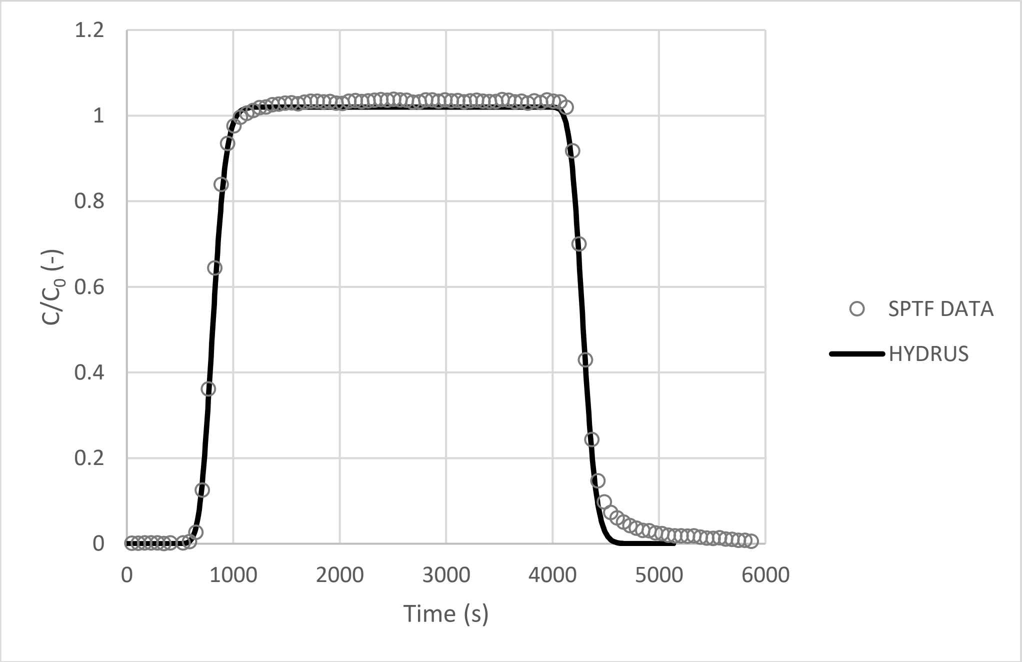

Figure 4.4- Tracer BTC in saturated conditions (Zn injection sand column). UV-vis spectrophotometer data and HYDRUS-1D modelling

Zinc transport

The zinc BTC in saturated sand is reported in Figure 4.5.

A good fitting is again observed after the HYDRUS modelling of the spectrophotometric results, especially in sorption and desorption. In Table 4.2 all the parameters obtained from the modelling are listed, together with the R squared value.

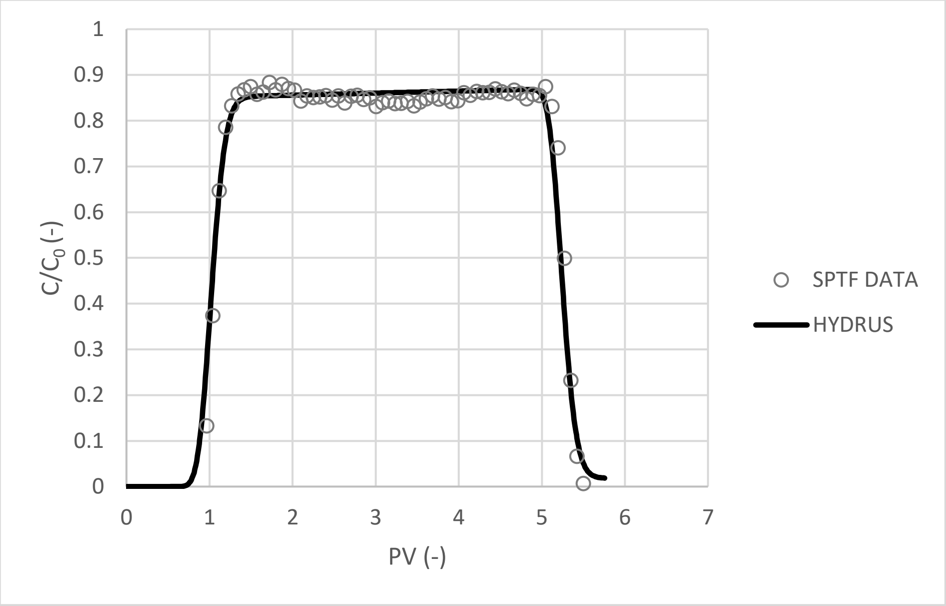

Figure 4.5- ZnCl2 BTC in saturated conditions. UV-vis spectrophotometer data and HYDRUS-1D modelling

Table 4.2- Modelling result of zinc injection BTC curve in saturated conditions

K_d (m^3/g)	ω (s^{-1})	R^2 (-)
$5.75 \cdot 10^{-7}$	$9.421 \cdot 10^{-5}$	0.99233

A comparison between zinc chloride and BFB breakthrough curves (Figure 4.6), highlights that the contaminant behaviour is similar to those of the tracer in sand material. The ascending and descending branches almost overlap. However, a certain interaction with the solid matrix happens, considering that the plateau occurs at values slightly lower than 1. To confirm this, the mass balance gave the results in Table 4.3, demonstrating that ≈15% is retained in the column.

Column tests were performed in parallel with the validation of the defined metals detection method. The BTC reconstructed with the Zinc-Zincon complexation is reported with the $ZnCl_2$ BTC in Figure 4.7. Looking at the graph, it can be concluded that the method is sufficiently precise, especially in the ascending and descending parts of the BTC. At plateau, instead, a value around 0.88 is observed.

Table 4.3- $ZnCl_2$ mass balance in saturated sand column

MASS IN (mmol)	56
MASS OUT (mmol)	47.5
% OUT	84.7

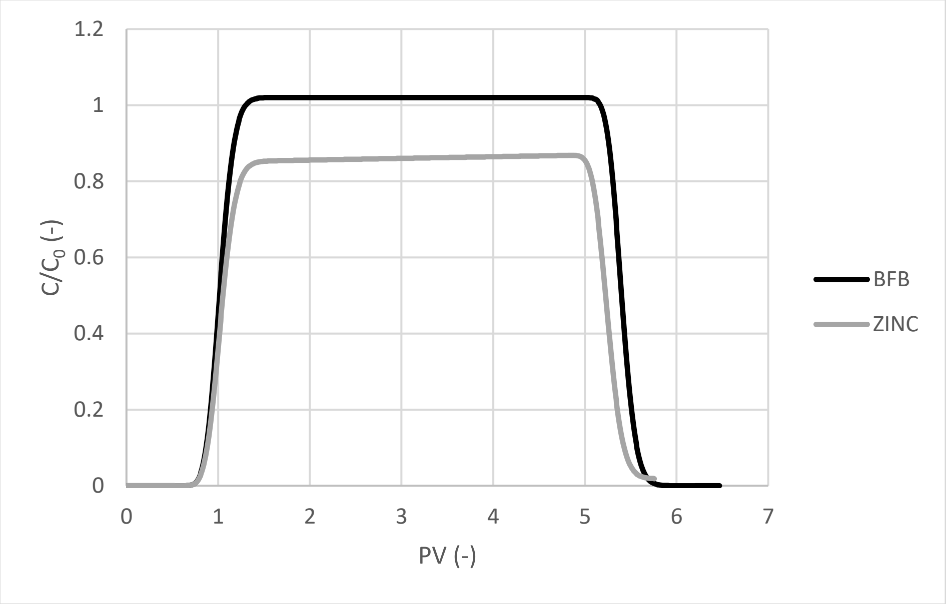

Figure 4.6- Tracer and ZnCl2 BTCs in saturated conditions. HYDRUS-1D modelling

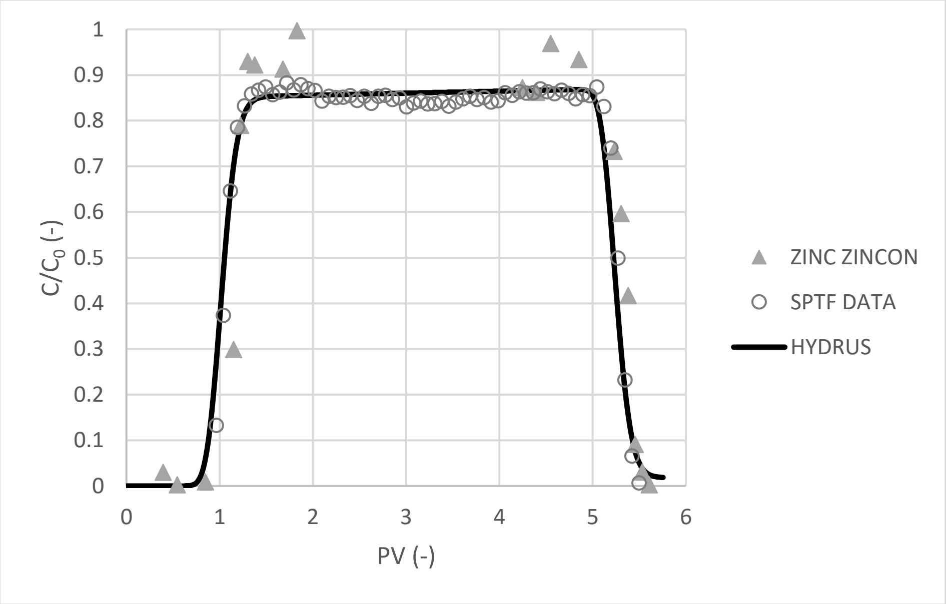

Figure 4.7- Comparison between reconstructed (with Zn-Zincon complexation method) and observed BTC in the saturated sand column

4.1.3.2 *Unsaturated conditions*

Bromophenol Blue BTC

In unsaturated conditions, the tracer test gave the result shown in Figure 4.8, in terms of BTC curve. The value retrieved for the pore volume is in Table 4.4. Pore volume is related to the total volume of voids in the porous medium and is calculated by multiplying the total volume by the effective porosity. This definition explains the lower value observed in unsaturated conditions with respect to saturated conditions. The other transport parameters are listed in the same table.

Table 4.4- Transport parameters obtained from BFB tracer test in unsaturated conditions (Zn injection column)

PV (min)	θ (-)	α_L (m)	K_s (m/s)	R^2 (-)
9.67	0.2936	$5.62 \cdot 10^{-3}$	$2.98 \cdot 10^{-4}$	0.99455

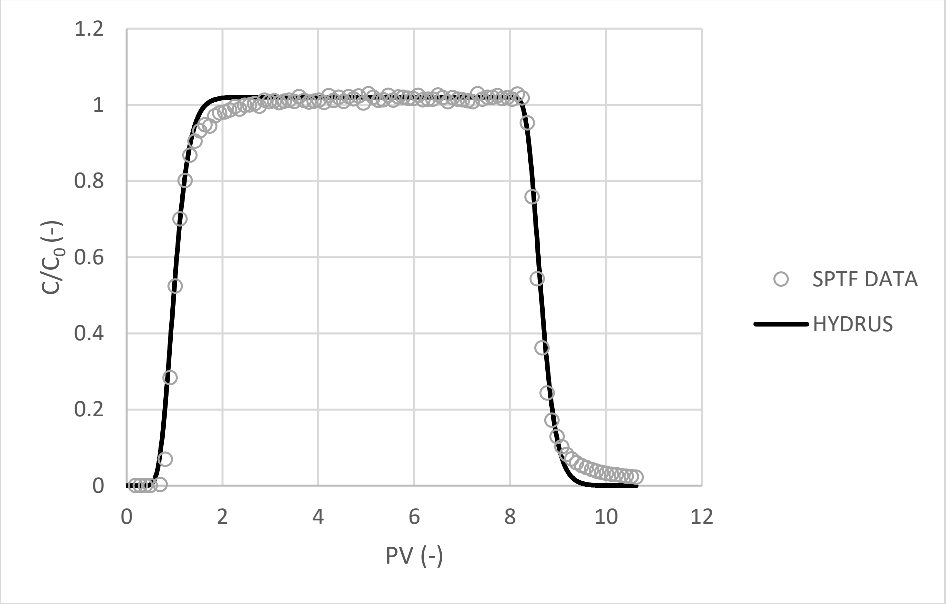

Figure 4.8- Tracer BTC in unsaturated conditions (Zn injection sand column). UV-vis spectrophotometer data and HYDRUS-1D modelling

Zinc transport

The modelling of zinc injection BTC (Figure 4.9) in the unsaturated sand column confirms the result obtained in saturated conditions.

In Figure 4.10, there is a direct comparison with the tracer BTC (the two curves are referred to tests with different duration). It is observed that, during the sorption zinc follows the same trend of the tracer, as in the desorption, while the $C/C_0 < 1$ explains that the contaminant remains attached to the sand, to a higher extent than the saturated test. The mass balance (Table 4.6) reveals in fact only ≈ 9% of retention.

Table 4.5- Modelling result of zinc injection BTC curve in unsaturated conditions

K_d (m^3/g)	ω (s^{-1})	R^2 (-)
$5.74 \cdot 10^{-7}$	$9.42 \cdot 10^{-5}$	0.99607

Table 4.6- $ZnCl_2$ mass balance in unsaturated sand column

MASS IN (mmol)	44
MASS OUT (mmol)	39.9
% OUT	90.6

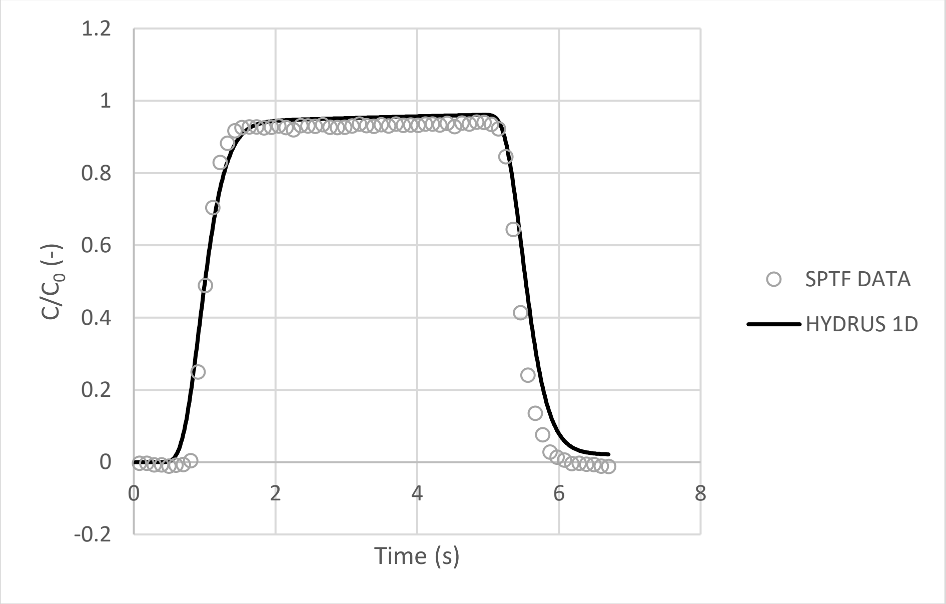

Figure 4.9- ZnCl2 BTC in unsaturated conditions. UV-vis spectrophotometer data and HYDRUS-1D modelling

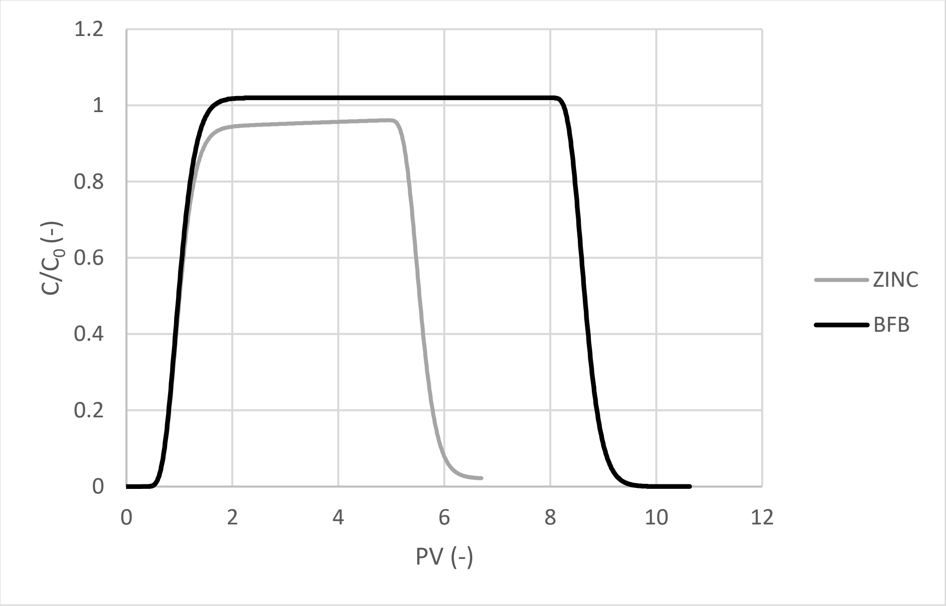

Figure 4.10- Tracer and ZnCl2 BTCs in unsaturated conditions. HYDRUS-1D modelling

The developed detection method for zinc has proved to be properly valid to quantitatively measure the contaminant also in unsaturated conditions. In Figure 4.11 the ascending and descending branches are well represented. The stationary level on the contrary presents the same problem of saturated conditions: a small but non-negligible scattering at high zinc concentrations.

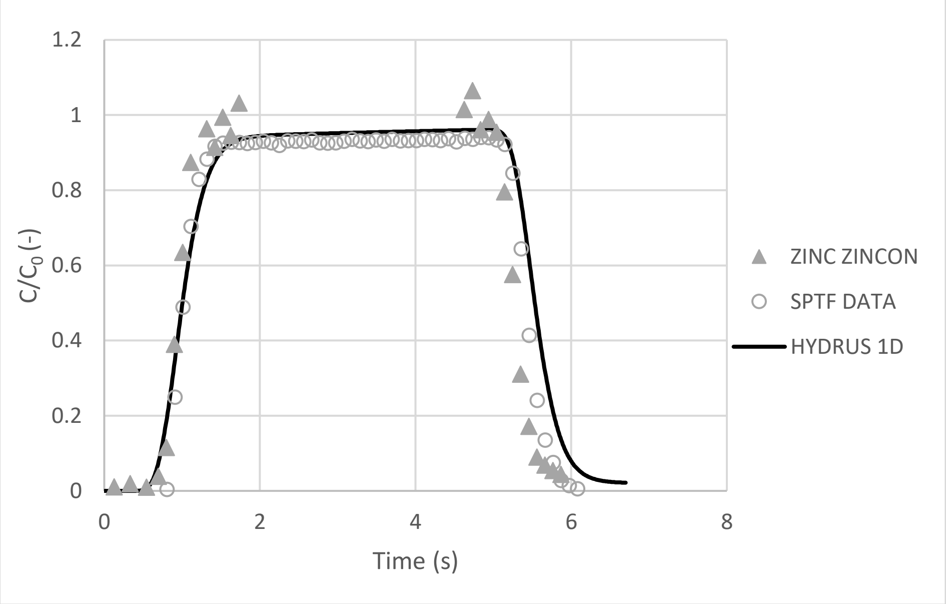

Figure 4.11- Comparison between reconstructed (with Zn-Zincon complexation method) and observed BTC in unsaturated sand column

4.1.4 Aluminium

4.1.4.1 Saturated conditions

Bromophenol Blue BTC

The saturated tracer test performed on this second sand-packed column provided the BTC drawn in Figure 4.12.

The pore volume retrieved from the experiment is slightly lower than the corresponding value in the other saturated column test. This is probably due to little variation in packing operations. The dispersivity parameter appears lower, while the saturated water content is increased, demonstrating differences in the porosity (Table 4.7).

Table 4.7- Transport parameters obtained from BFB tracer test in saturated conditions (Zn injection column)

PV (min)	θ_s (-)	α_L (m)	R^2 (-)
16.80	0.4965	$1.01 \cdot 10^{-3}$	0.99937

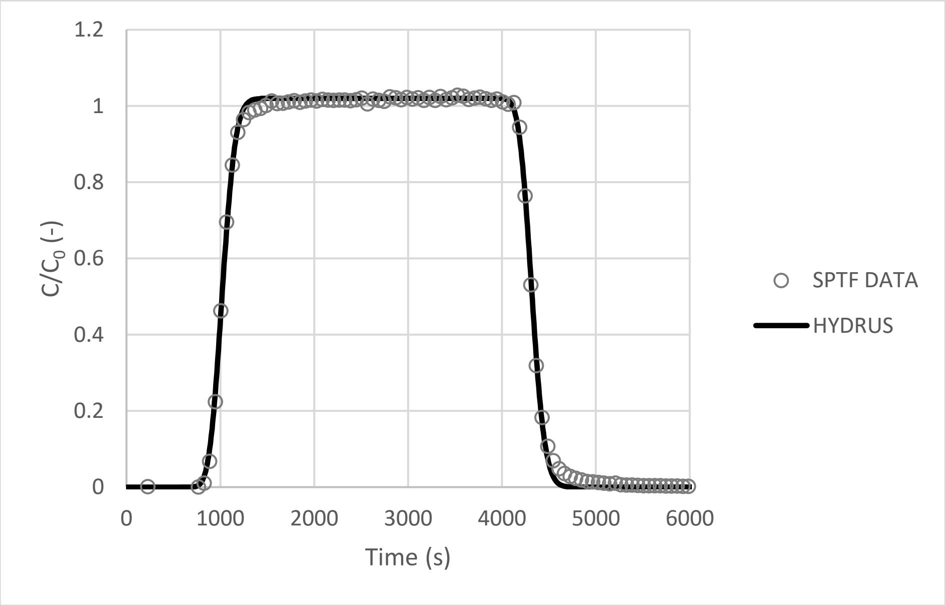

Figure 4.12- Tracer BTC in saturated conditions (Al injection sand column). UV-vis spectrophotometer data and HYDRUS-1D modelling

Aluminium transport

The data fitting in HYDRUS-1D continues to be satisfactory also for saturated $AlCl_3$ injection study. The modelling results are shown in Table 4.8 and the modelled tracer BTC in Figure 4.13.

By comparing the aluminium and the tracer BTCs (Figure 4.14) the values of the parameters in table acquire significance: the absence of retardation is evident, with the sorption lines that increase together until stationarity, as well as the desorption part.

Table 4.8- Modelling result of aluminium injection BTC curve in saturated conditions

K_d (m^3/g)	ω (s^{-1})	R^2 (-)
$2.49 \cdot 10^{-5}$	$2.51 \cdot 10^{-7}$	0.99486

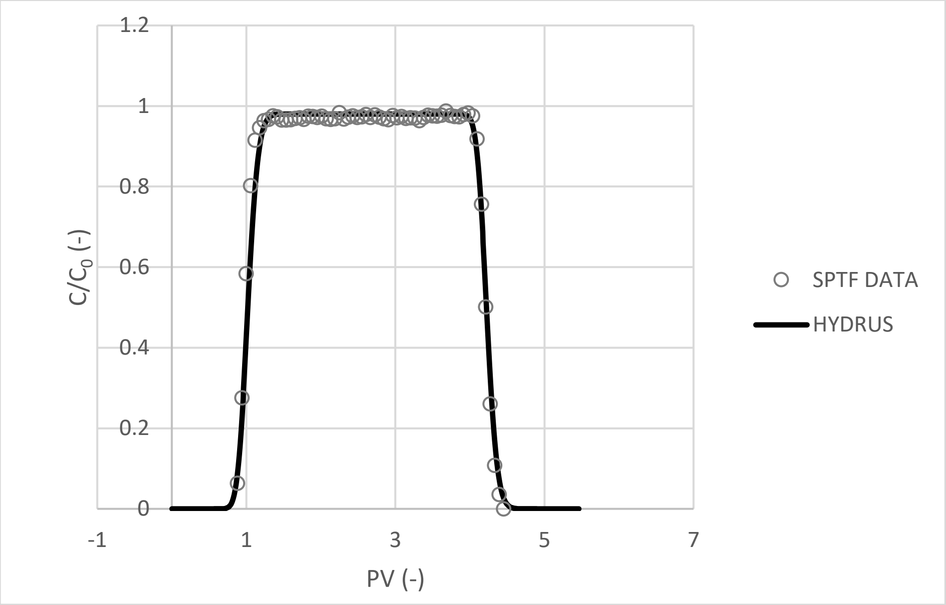

Figure 4.13- $AlCl_3$ BTC in saturated conditions. UV-vis spectrophotometer data and HYDRUS-1D modelling

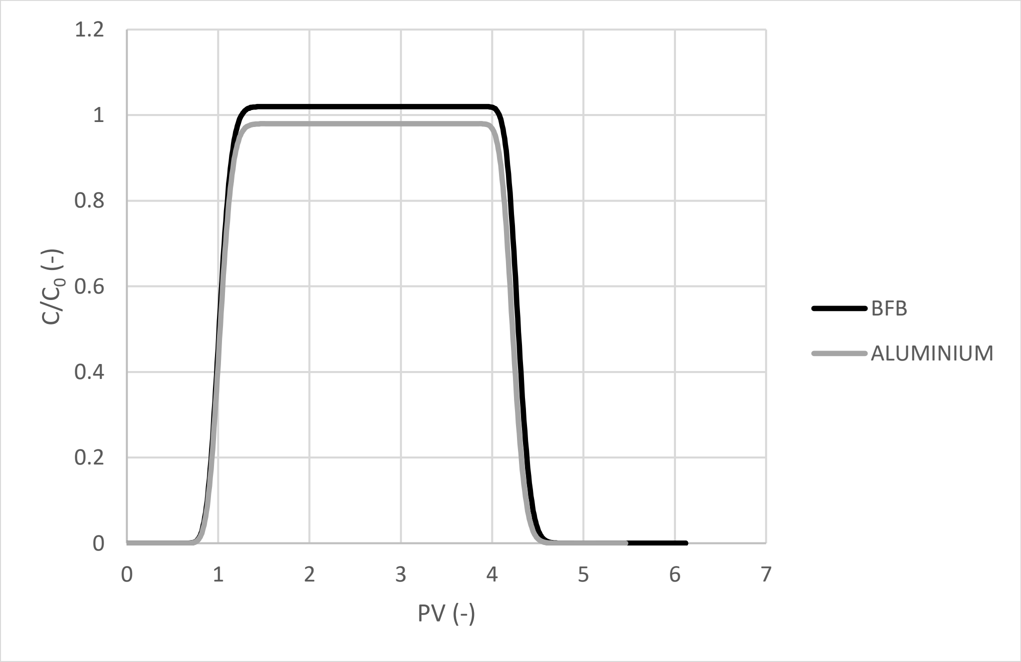

Figure 4.14- Tracer and $AlCl_3$ BTCs in saturated conditions. HYDRUS-1D modelling

Retention is observed this time, too, even though it is not so significant: C/C_0 values at plateau are very close to 1 and the performed mass balance, in Table 4.9, suggests a retention percentage of ≈ 3%.

Table 4.9- $AlCl_3$ mass balance in saturated sand column

MASS IN (mmol)	893
MASS OUT (mmol)	862
% OUT	96.6

The detection analysis based on aluminium-pyrocatechol violet complexation enabled to reconstruct the breakthrough curve in Figure 4.15. What has already seen in the previous discussion is again observed: the method is able to detect well the concentrations in the ascending and descending part, but it is less accurate at the plateau.

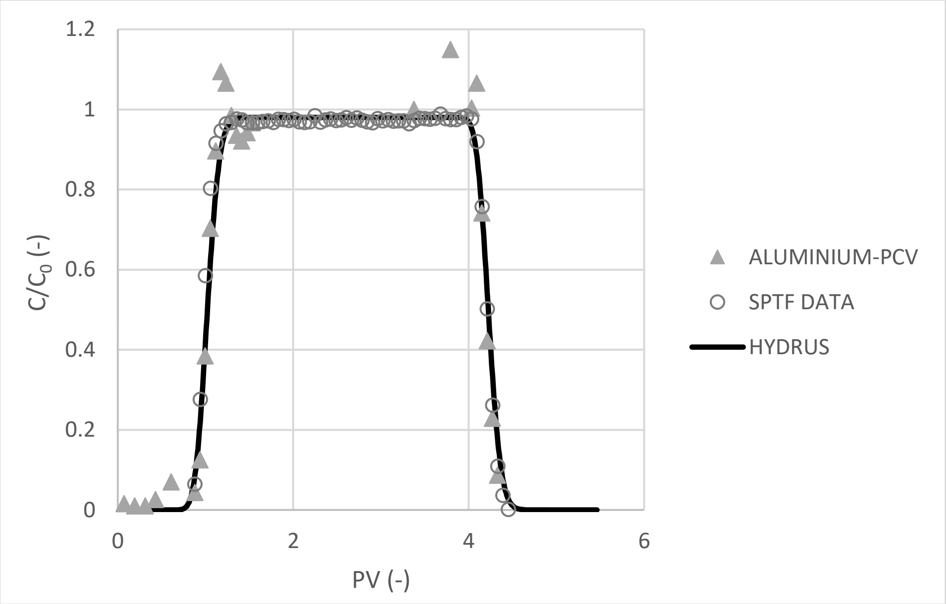

Figure 4.15- Comparison between reconstructed (with Al-PV complexation method) and observed BTC in saturated sand column

4.1.4.2 Unsaturated conditions

Bromophenol Blue BTC

In Figure 4.16 the result of the unsaturated tracer test modelling is shown. The characteristic pore volume along with the other transport parameters obtained from the modelling are listed in Table 4.10.

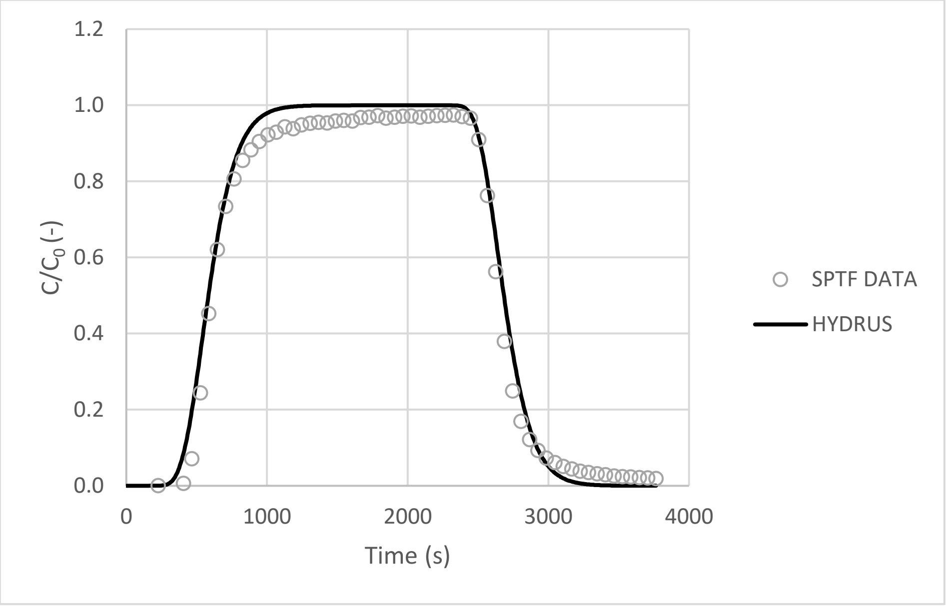

Figure 4.7- Tracer BTC in unsaturated conditions (Al injection sand column). UV-vis spectrophotometer data and HYDRUS-1D modelling

Table 4.10- Transport parameters obtained from BFB tracer test in unsaturated conditions (Zn injection column)

PV (min)	θ (-)	α_L (m)	Ks (m/s)	R^2 (-)
9.83	0.3011	$6.36 \cdot 10^{-3}$	$5.84 \cdot 10^{-4}$	0.99403

Aluminium transport

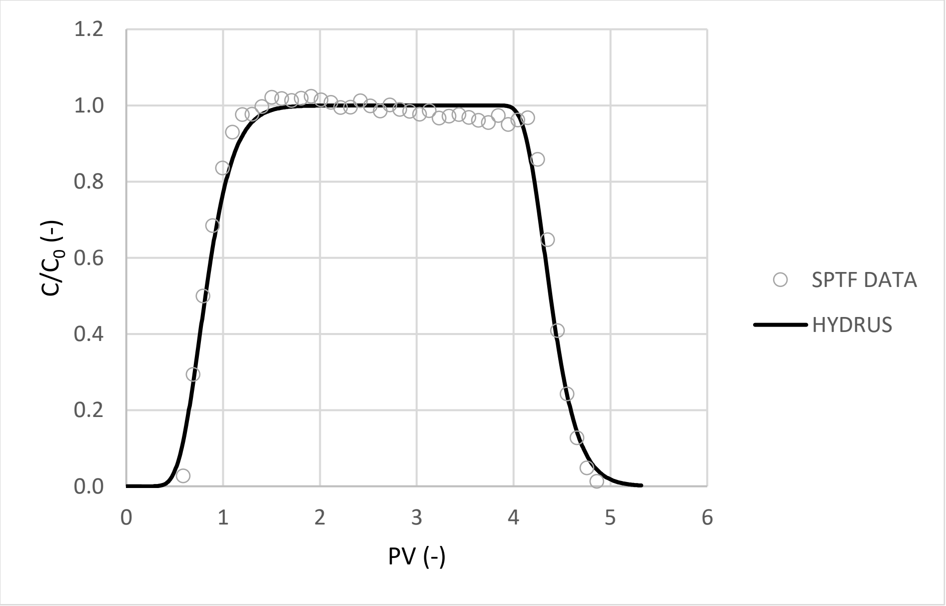

Figure 4.8- $AlCl_3$ BTC in unsaturated conditions. UV-vis spectrophotometer data and HYDRUS-1D modelling

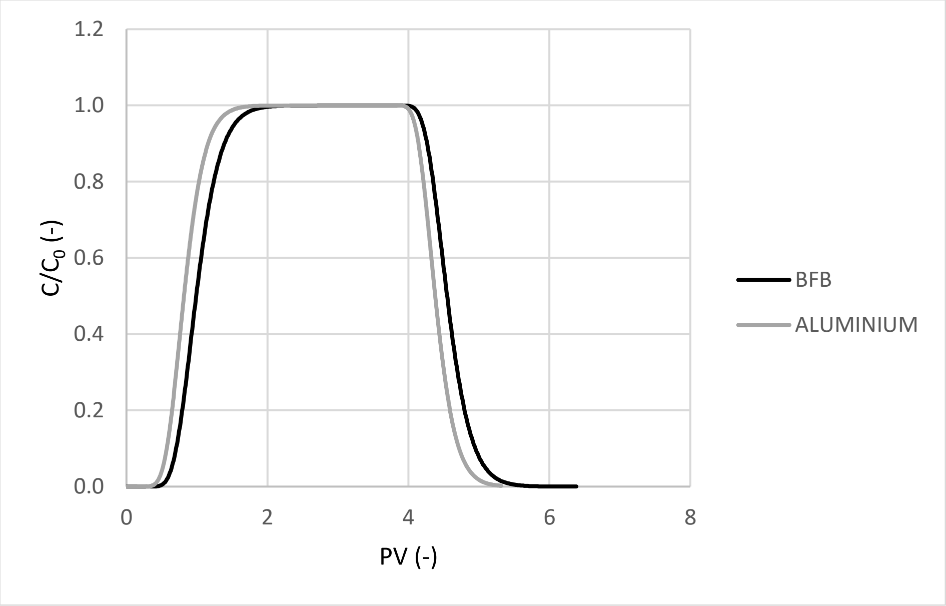

Figure 4.18- Tracer and $AlCl_3$ BTCs in unsaturated conditions. HYDRUS-1D modelling

Figure 4.17 shows the modelled $AlCl_3$ BTC and in Table 4.11 the reaction parameters are reported. In all the tests carried out in unsaturated sand columns, aluminium behaves in unusual ways, as highlighted by the comparison with the respective tracer BTC (Figure 4.18). This unexpected behaviour is probably determined by the sand column being altered by the aluminium transit in saturated conditions. The mass balance (Table 4.12) proves that all the injected aluminium leaves the column.

Table 4.11- Modelling result of aluminium injection BTC curve in saturated conditions

K_d (m^3/g)	ω (s^{-1})	R^2 (-)
$1.503 \cdot 10^{-8}$	1	0.99203

Table 4.12- $AlCl_3$ mass balance in unsaturated sand column

MASS IN (mmol)	62.8
MASS OUT (mmol)	62.7
% OUT	99.9

The irregularity of aluminium behaviour in unsaturated conditions is observed also at the UV-vis spectrophotometric detection with complexation with PV reactant. The resulting BTC, shown in Figure 4.19, demonstrates that the colorimetric method fails in reconstructing all the steps of the BTC.

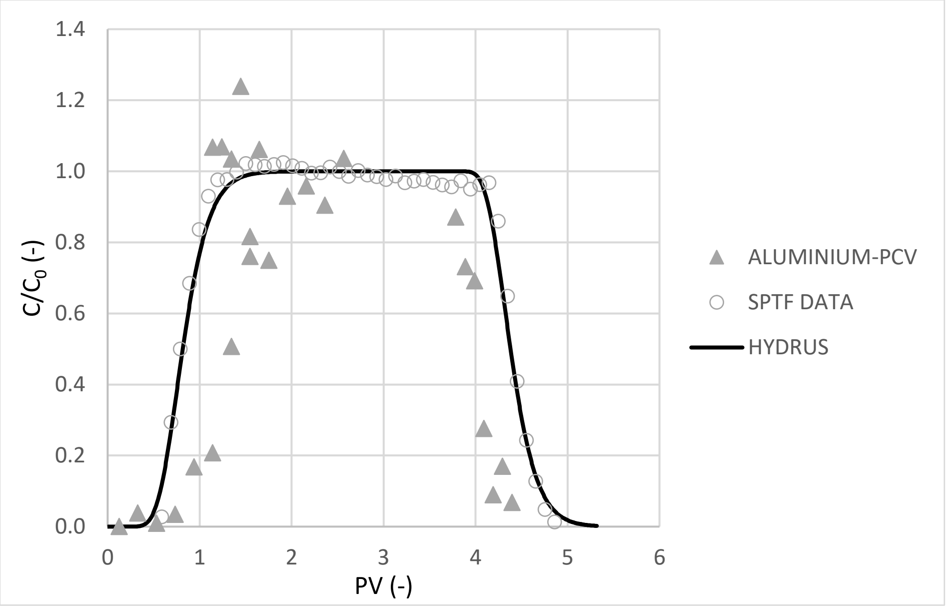

Figure 4.19- Comparison between reconstructed (with Al-PV complexation method) and observed BTC in unsaturated sand column

4.2 Soil-packed column tests

The results of unsaturated tracer tests performed on soil-packed columns are reported in Figure 4.20 and Figure 4.21. As it can be noted, BFB has essentially the same behaviour in sand and standard soil. The retrieved pore volumes in both cases are in the same order of magnitude than in sand-packed columns. The same for the other parameters listed in Table 4.11 and Table 4.12.

Table 4.10- - Transport parameters obtained from BFB tracer test in unsaturated conditions (Zn injection soil-column)

PV (min)	θ (-)	α_L (m)	Ks (m/s)	R^2 (-)
13.76	0.4767	$5.71 \cdot 10^{-3}$	$1.48 \cdot 10^{-3}$	0.99742

Table 4.12- - Transport parameters obtained from BFB tracer test in unsaturated conditions (Al injection soil-column)

PV (min)	θ (-)	α_L (m)	Ks (m/s)	R^2 (-)
12.76	0.557	$7.65 \cdot 10^{-3}$	$1.51 \cdot 10^{-3}$	0.9978

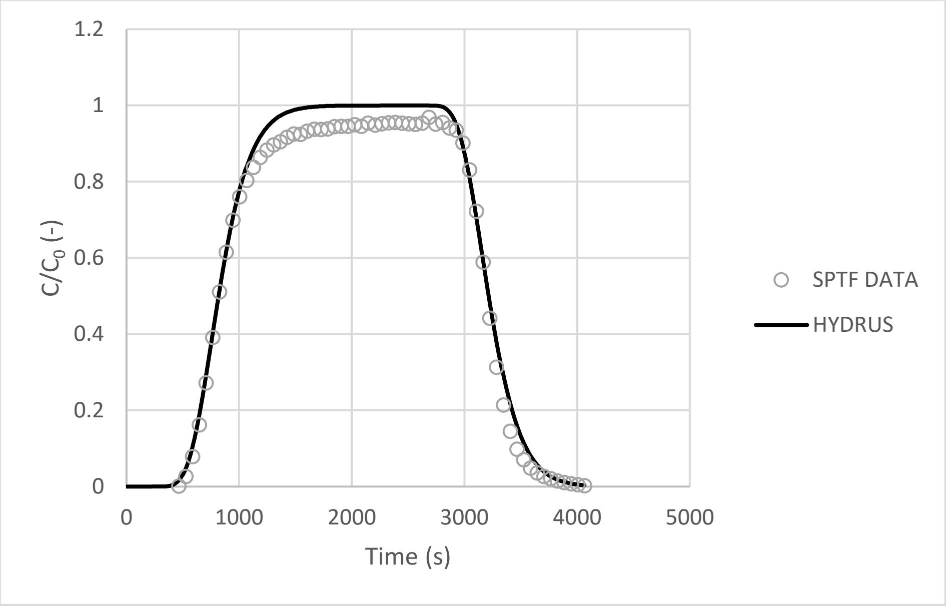

Figure 4.20- Tracer BTC in unsaturated conditions (Zn injection soil column). UV-vis spectrophotometer data and HYDRUS-1D modelling

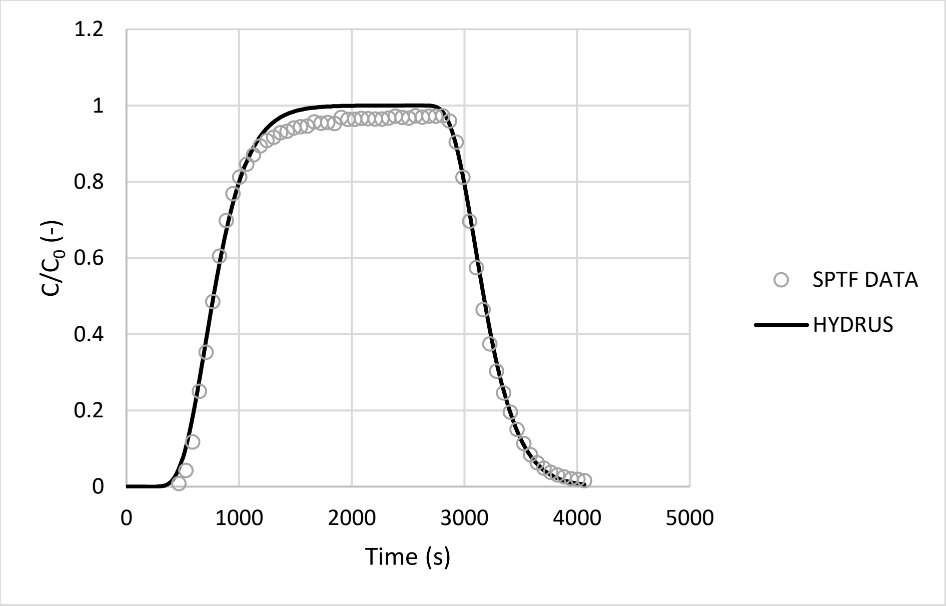

Figure 4.21- Tracer BTC in unsaturated conditions (Al injection soil column). UV-vis spectrophotometer data and HYDRUS-1D modelling

The metals' transport in unsaturated soil has the trend shown in Figure 4.19 and Figure 4.20 for zinc and aluminium respectively.

The BTCs are reconstructed exclusively from colorimetric detection on punctual samples. Moreover, due to the high retardation factor estimated in batch tests, experiments on soil were conducted on a time-period of 24 h, by sampling at a frequency of 25 minutes. Then, on the sampled 25 µL complexation operations took place. HYDRUS 1D modelling of zinc injection in unsaturated soil column considers a linear sorption with chemical non-equilibrium given by the first-order kinetic degradation (SNKL1). Aluminium BTC was modelled like on sand material.

The determined values of the retardation factors (listed Table 4.13 and 4.14), suggest that the overlapping with the BTCs of the respective tracer tests is poorly informative in both cases. $C/C_0 = 0.5$ requests 13 PV to be reached for zinc, while 8 PV for aluminium.

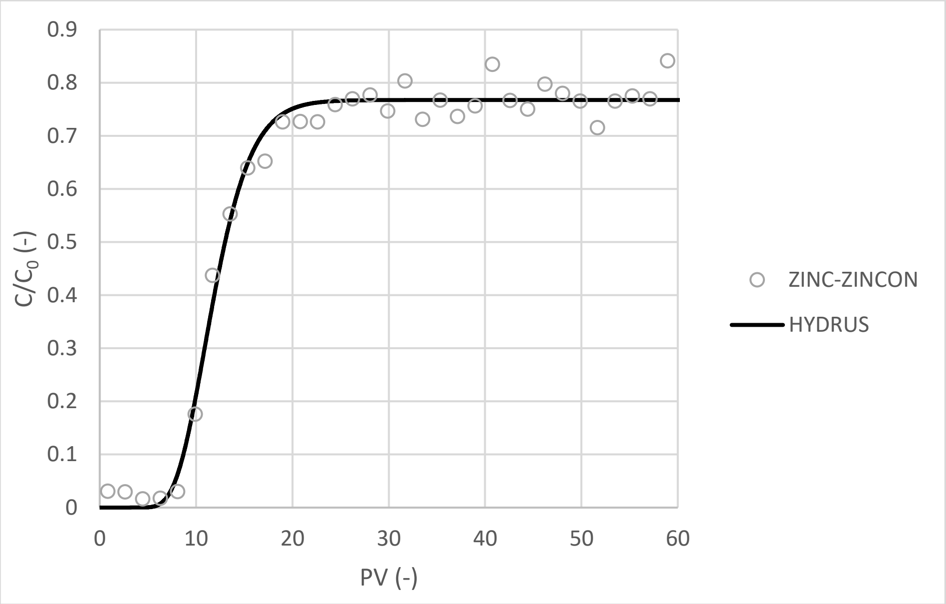

Figure 4.22- Zinc BTC in unsaturated soil determined through Zn-ZINCON complexation

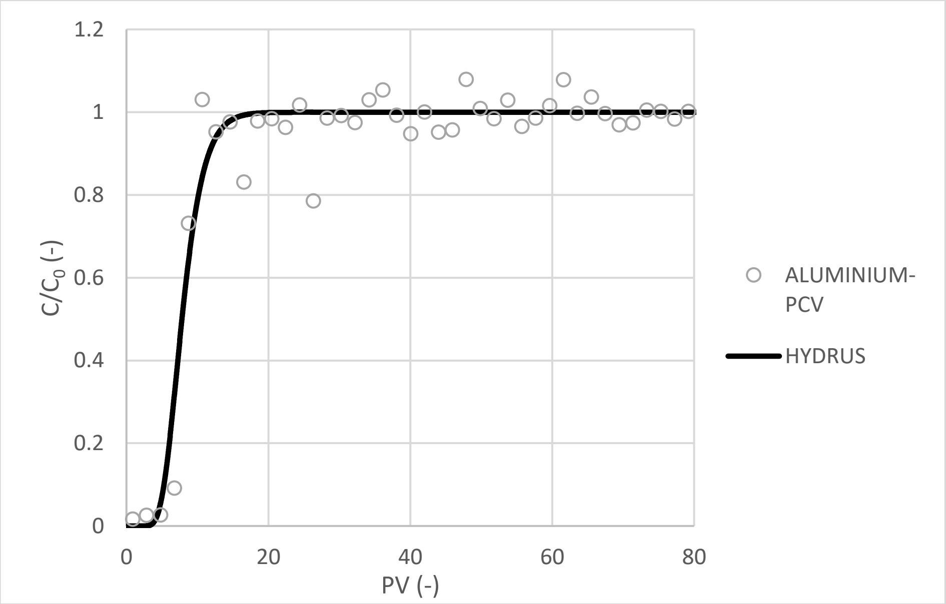

Figure 4.23- Aluminium BTC in unsaturated soil determined through Al-PCV complexation

Table 4.13- Modelling result of zinc injection BTC curve in unsaturated soil

K_d (m^3/g)	ω (s^{-1})	SNKL1 (s^{-1})	R (-)	R^2 (-)
$3.53 \cdot 10^{-6}$	0.1814	$3.16 \cdot 10^{-4}$	12	0.9873

Table 4.11- Modelling result of aluminium injection BTC curve in unsaturated soil

K_d (m^3/g)	ω (s^{-1})	R (-)	R^2 (-)
$2.09 \cdot 10^{-6}$	0.4252	6.73	0.93854

4.3 Simulation of zinc release from mining waste

In Figure 4.23, the BTC resulted from the pulse injection of mining waste is reported. In the graph the released material is described as mass of Zn^{2+} ion. The test is performed in a pH 3.6 sand column, with a rougher mixture at the same pH. After the injection a sharp increase in the released material is observed in the next 2 minutes. A slower release characterizes the next 5.5 minutes, with a progressive reduction of concentration up to values close to zero. After the flushing with deionized water, a new release of substance is observed, probably determined by changes in pH, that cause the movement of previously adsorbed particles. Considering the material composition, the Zn^{2+} presence in the material resulted equal to 3560 mg. As indicated in Table 4.14 after the injection ≈ 0.062 % of Zn^{2+} is released, to reach little more than 0.09 % after flushing.

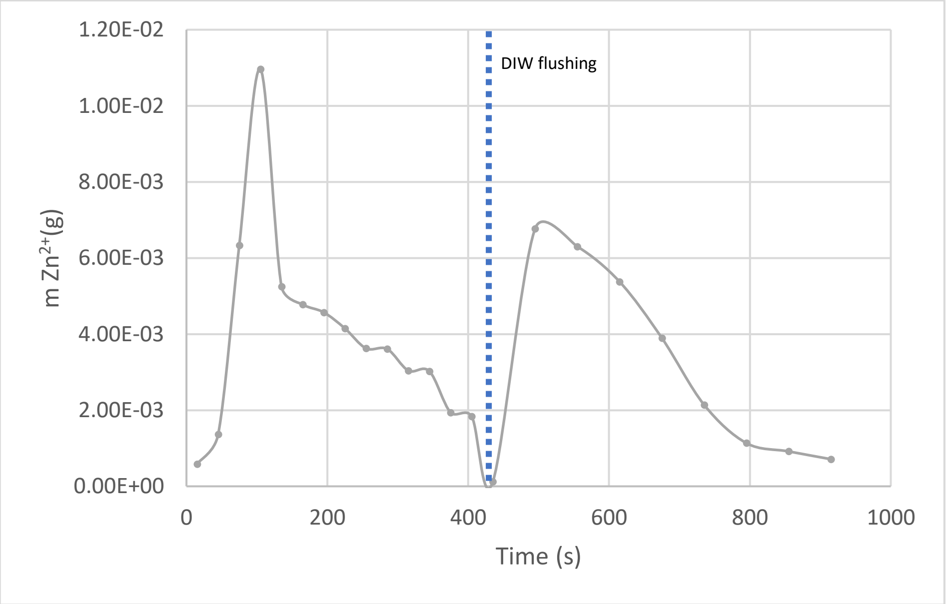

Figure 4.24- BTC pulse injection of rougher material. The dashed line indicates the start of flushing with DIW

To conclude, the mobilization happens at a slow rate, and it is highly affected by the pH of the infiltrating water. Elaboration of batch tests realized on other pH values reveals, for the same mass of waste material (1780 mg Zn^{2+}), a dissolution of Zn^{2+} in the percentage reported in Table 4.16.

Table 4.15- Zn^{2+} release after injection and after DIW flushing

	INJECTION STEP	FLUSHING STEP
RELEASED MASS (mg)	2.21	3.3
% RELEASE	$6.20 \cdot 10^{-2}$	$3.06 \cdot 10^{-2}$

Table 4.16- Effect of the pH in the Zn^{2+} mobilization

	DIW	pH 4.5	pH 3.6
RELEASED MASS (mg)	0.446829	0.72755	1.557486
% RELEASE	$2.51 \cdot 10^{-4}$	$4.09 \cdot 10^{-4}$	$8.75 \cdot 10^{-4}$

5 Conclusions

This thesis aimed to reconstruct the behaviour in the soil of two target contaminants, zinc and aluminium, studied as chloride solutions. Column and batch tests were performed for this purpose.

Column experiments allowed studying the transport in unsaturated conditions (vadose zone), after a preliminary characterization in saturated conditions (groundwater environment). Saturated and unsaturated tests on sand columns were carried out as the first step, before moving to soil-packed columns, where only the unsaturated environment has been investigated. In general, the results expressed as BTCs suggest the strong mobility of both zinc and aluminium. Going into detail, zinc tents more than aluminium to be adsorbed on a solid support, less in unsaturated than saturated conditions. Limited to sand columns, the percentage of release varies from 90% of the vadose zone to more than 80% of the saturated conditions. In standard soil, it exhibits a strong delay, though maintaining the same behaviour in terms of retention. For what concern aluminium, sand-column tests show that it is always very mobile, particularly in unsaturated sand columns, where almost 100% of the injected material is released. Soil column experiment confirms this behaviour and highlights retardation, which, although less severe than for zinc, is considerable.

Batch tests were used to determine the sorptive behaviour of the two studied metals before the soil-packed column tests. Zinc is characterized by Langmuir sorption isotherm. Aluminium behaviour is well described by linear isotherm. The calculated R factor are not confirmed by column tests on soil. It can be concluded that batch tests over esteem and under esteem the retardation in the case of aluminium and zinc, respectively.

A central part of this work was the development and the validation of colorimetric methods for Zn and Al detection. Methods found in the literature were used as the basis to develop consistent, effective, but also easy and safe protocols. These detection techniques exploit complexation reactions with selective ligands on samples manually collected at a selected frequency. The method proved to be rather accurate in the ascending and descending parts of the BTCs, less at the plateau.

In the last part, to simulate real contamination, a pulse injection of mining waste enriched in zinc has been done on an unsaturated sand column. The pH value of the column was modified to reach acidic values in order to recreate the optimal environment for Zn^{2+} mobilization. The typical path of an impulsive injection was observed, but with a limited Zn^{2+} release.

To conclude, according to sand column tests groundwater may be threatened by zinc and aluminium discharge on topsoil since they show a tracer-like behaviour, but interaction mechanisms can slow down the spread in soils.

To improve the knowledge on these two contaminants’ behaviour across the vadose zone, further studies can be done, investigating other scales for analysis, using different metals’ concentrations and/or using other porous media as solid material (i.e. natural soil).

References

Abdulla, F. (2016). *Determination of zinc ions in drinking water distribution systems (PVC pipes) by spectrophotometric method*.

Arancibia, V, Zúñiga, M., Zúñiga, M. C., Segura, R., & Esteban, M. (2010). Optimization of Experimental Parameters in the Determination of Zinc in Sea Water by Adsorptive Stripping Voltammetry. In J. Braz. Chem. Soc (Vol. 21, Issue 2).

Arancibia, Verónica, & Muñoz, C. (2007). Determination of aluminium in water samples by adsorptive cathodic stripping voltammetry in the presence of pyrogallol red and a quaternary ammonium salt. *Talanta*, *73*(3), 546–552. doi: 10.1016/j.talanta.2007.04.009

Bear, J. J., & Cheng, H.-D. A. (2010). Unsaturated Flow Models. In Modeling Groundwater Flow and Contaminant Transport (pp. 251–340). Springer Netherlands. doi: 10.1007/978-1-4020-6682-5_6

Beauchemin, D. (2008). Inductively coupled plasma mass spectrometry. In Analytical Chemistry (Vol. 80, Issue 12, pp. 4455–4486). doi: 10.1021/ac8006945

Behroozi, A., Arora, M., Fletcher, T. D., & Western, A. W. (2020). Sorption and transport behavior of zinc in the soil; Implications for stormwater management. *Geoderma*, *367*. doi: 10.1016/j.geoderma.2020.114243

Bradl, H. B. (2005). Sources and origins of heavy metals. In Interface science and technology (Vol. 6, pp. 1–27). Elsevier.

Brooks, R., & Corey, T. (1964). Hydraulic properties of porous media. *Hydrology Papers, Colorado State University*, *24*, 37.

Burdine, N. T. (1953). Relative Permeability Calculations From Pore Size Distribution Data. *Journal of Petroleum Technology*, *5*(03), 71–78. doi: 10.2118/225-G

Campbell, A., Becaria, A., Lahiri, D. K., Sharman, K., & Bondy, S. C. (2004). *Chronic Exposure to Aluminum in Drinking Water Increases Inflammatory Parameters Selectively in the Brain*.

Carletto, J. S., Roux, K. C. D. pietro, Maltez, H. F., Martendal, E., & Carasek, E. (2008). Use of 8-hydroxyquinoline-chitosan chelating resin in an automated on-line preconcentration system for determination of zinc (II) by F AAS. *Journal of Hazardous Materials*, *157*(1), 88–93.

Chow, C. W. K., Thomas, S. D., Davey, D. E., Mulcahy, D. E., & Drikas, M. (2003). Development of an on-line electrochemical analyser for trace level aluminium. *Analytica Chimica Acta*, *499*(1–2), 173–181. doi: 10.1016/j.aca.2003.08.028

Cronan, C. S., & Schofield, C. L. (1979). Aluminum leaching response to acid precipitation: effects on high-elevation watersheds in the northeast. *Science*, *204*(4390), 304–306.

Dagan, G. (1984). Solute transport in heterogeneous porous formations. *Journal of Fluid Mechanics*, *145*, 151–177.

DESA, U. N. (2019). World Urbanization Prospects 2018: Highlights (ST/ESA/SER. A/421. United Nations, Department of Economic and Social Affairs (UN DESA). *Population Division, New York, NY, USA*.

Ediger, R. D., & Fernandez, F. J. (1980). Optimization of ICP (Inductively Coupled Plasma) Background Correction Param-eters. *At. Spectrosc*, *1*, 1.

Epstein, M. S., Rains, T. C., Brady, T. J., Moody, J. R., & Barnes, I. L. (1978). Determination of Several Trace Metals in Simulated Fresh Water by Graphite Furnace Atomic Emission Spectrometry. *Analytical Chemistry*, *50*(7), 874–880. doi: 10.1021/ac50029a015

Farghaly, O. A., Hameed, R. S. A., & Abu-Nawwas, A.-A. H. (2014). Analytical Application Using Modern Electrochemical Techniques. In Int. J. Electrochem. Sci (Vol. 9). Retrieved from www.electrochemsci.org

Fernández-Calviño, D., Pérez-Novo, C., Bermúdez-Couso, A., López-Periago, E., & Arias-Estévez, M. (2010). Batch and stirred flow reactor experiments on Zn sorption in acid soils. Cu competition. *Geoderma*, *159*(3–4), 417–424. doi: 10.1016/j.geoderma.2010.09.007

Fernández-Sánchez, M. L. (2019). Atomic emission spectrometry | inductively coupled plasma. In Encyclopedia of Analytical Science (pp. 169–176). Elsevier. doi: 10.1016/B978-0-12-409547-2.14542-1

Flaten, T. P. (2001). *Aluminium as a risk factor in Alzheimer's disease, with emphasis on drinking water*.

Fonseca, B., Figueiredo, H., Rodrigues, J., Queiroz, A., & Tavares, T. (2011). Mobility of Cr, Pb, Cd, Cu and Zn in a loamy sand soil: A comparative study. *Geoderma*, *164*(3–4), 232–237. doi: 10.1016/j.geoderma.2011.06.016

Frankowski, M., Zioła-Frankowska, A., & Siepak, J. (2010). New method for speciation analysis of aluminium fluoride complexes by HPLC-FAAS hyphenated technique. *Talanta*, *80*(5), 2120–2126. doi: 10.1016/j.talanta.2009.11.018

Freeze, R. A., & Cherry, J. A. (1979). *Groundwater*.

Imperato, M., Adamo, P., Naimo, D., Arienzo, M., Stanzione, D., & Violante, P. (2003). Spatial distribution of heavy metals in urban soils of Naples city (Italy). *Environmental Pollution*, *124*(2), 247–256. doi: 10.1016/S0269-7491(02)00478-5

Irsa-Cnr, A. (2003). Metodi analitici per le acque. *APAT Manuali e Linee Guida*, *29*, 2003.

Jellali, S., Diamantopoulos, E., Kallali, H., Bennaceur, S., Anane, M., & Jedidi, N. (2010). Dynamic sorption of ammonium by sandy soil in fixed bed columns: Evaluation of equilibrium and non-equilibrium transport processes. *Journal of Environmental Management*, *91*(4), 897–905. doi: 10.1016/j.jenvman.2009.11.006

Jellali, Salah, Benremita, H., Muntzer, P., Razakarisoa, O., & Schäfer, G. (2003). A large-scale experiment on mass transfer of trichloroethylene from the unsaturated zone of a sandy aquifer to its interfaces. *Journal of Contaminant Hydrology*, *60*(1–2), 31–53.

Jones, D. L., Gilroy, S., Larsen, P. B., Howell, S. H., & Kochian, L. v. (1998). Effect of aluminum on cytoplasmic Ca2+ homeostasis in root hairs of Arabidopsis thaliana (L.). *Planta*, *206*(3), 378–387.

Kefala, G., Economou, A., Voulgaropoulos, A., & Sofoniou, M. (2003). A study of bismuth-film electrodes for the detection of trace metals by anodic stripping voltammetry and their application to the determination of Pb and Zn in tapwater and human hair. *Talanta*, *61*(5), 603–610. doi: 10.1016/S0039-9140(03)00350-3

Khorshid, M. S. H., & Thiele-Bruhn, S. (2016). Contamination status and assessment of urban and non-urban soils in the region of Sulaimani City, Kurdistan, Iraq. *Environmental Earth Sciences*, *75*(16). doi: 10.1007/s12665-016-5972-z

Korenaga, T., Motomizu, S., & Tôei, K. (1980). Extraction-spectrophotometric determination of aluminium in river water with pyrocatechol violet and a quaternary ammonium salt. *Talanta*, *27*(1), 33–38.

Krawczyk, M., Jeszka-Skowron, M., & Matusiewicz, H. (2014). Sequential multi-element determination of iron and zinc in water samples by high-resolution continuum source graphite furnace atomic absorption spectrometry after column solid-phase extraction onto multiwalled carbon nanotubes. *Microchemical Journal*, *117*, 138–143. doi: 10.1016/j.microc.2014.06.023

Li, X., & Huang, C. (2007). Environment impact of heavy metals on urban soil in the vicinity of industrial area of Baoji city, P.R. China. *Environmental Geology*, *52*(8), 1631–1637. doi: 10.1007/s00254-006-0608-3

Lian, H., Kang, Y., Bi, S., Arkin, Y., Shao, D., Li, D., Chen, Y., Dai, L., Gan, N., & Tian, L. (2004). Direct determination of trace aluminum with quercetin by reversed-phase high performance liquid chromatography. *Talanta*, *62*(1), 43–50. doi: 10.1016/S0039-9140(03)00405-3

Martin-Esteban, A., Fernhdez, P., Phez-Conde, C., Gutikrrez, A., & Cimara, C. (1995). CHIMICA ACTA ELSEVIER On-line preconcentration of aluminium with immobilized Chromotrope 2B for the determination by flame atomic absorption spectrometry and inductively coupled plasma mass spectrometry. In Analytica Chimica Acta (Vol. 304).

Mason, Y., Ammann, A. A., Ulrich, A., & Sigg, L. (1999). Behavior of heavy metals, nutrients, and major components during roof runoff infiltration. *Environmental Science and Technology*, *33*(10), 1588–1597. doi: 10.1021/es980922q

Matúš, P., Hagarová, I., Bujdoš, M., Diviš, P., & Kubová, J. (2009). Determination of trace amounts of total dissolved cationic aluminium species in environmental samples by solid phase extraction using nanometer-sized titanium dioxide and atomic spectrometry techniques. *Journal of Inorganic Biochemistry*, *103*(11), 1473–1479. doi: 10.1016/j.jinorgbio.2009.08.004

Mesquita, R. B. R., & Rangel, A. O. S. S. (2008). Development of Sequential Injection Methodologies for the Spectrophotometric Direct and Kinetic Determination of Aluminium in Natural and Waste Waters. In J. Braz. Chem. Soc (Vol. 19, Issue 6).

MiPAF. (2001). *Metodi di analisi delle acque per uso agricolo e zootecnico.* (Franco Angeli, Ed.). Milano.

Moldovan, M. (2019). Atomic Absorption Spectrometry-Flame. In Encyclopedia of Analytical Science (pp. 129–136). Elsevier. doi: 10.1016/B978-0-12-409547-2.00022-6

Mualem, Y. (1976). *A New Model for Predicting the Hydraulic Conductivity of Unsaturated Porous Media* (Vol. 12, Issue 3).

Narin, I., Tuzen, M., & Soylak, M. (2004). Aluminium determination in environmental samples by graphite furnace atomic absorption spectrometry after solid phase extraction on Amberlite XAD-1180/pyrocatechol violet chelating resin. *Talanta*, *63*(2), 411–418. doi: 10.1016/j.talanta.2003.11.005

Nielsen, D. R., van Genuchten, M. T., & Biggar, J. W. (1986). Water Flow and Solute Transport Processes in the Unsaturated Zone. In WATER RESOURCES RESEARCH (Vol. 22, Issue 9).

Nimmo, J. R. (2005). Unsaturated Zone Flow Processes. In Encyclopedia of Hydrological Sciences. John Wiley & Sons, Ltd. doi: 10.1002/0470848944.hsa161

Orians, K. J., & Bruland, K. W. (1986). The biogeochemistry of aluminum in the Pacific Ocean. *Earth and Planetary Science Letters*, *78*(4), 397–410.

Parker, J. C. (1989). Multiphase flow and transport in porous media. *Reviews of Geophysics*, *27*(3), 311–328.

Paus, P. E. (1973). Determination of some heavy metals in sea water by atomic absorption spectrophotometry. *Fresenius' Zeitschrift Für Analytische Chemie*, *264*(2), 118–122.

Préndez, M., & Carrasco, M. A. (2003). *ELEMENTAL COMPOSITION OF SURFACE WATERS IN THE ANTARCTIC PENINSULA AND INTERACTIONS WITH THE ENVIRONMENT*.

Rahman, R., & Upadhyaya, H. (2021). Aluminium Toxicity and Its Tolerance in Plant: A Review. In Journal of Plant Biology (Vol. 64, Issue 2, pp. 101–121). Springer Science and Business Media Deutschland GmbH. doi: 10.1007/s12374-020-09280-4

Rezaee, M., Yamini, Y., Khanchi, A., Faraji, M., & Saleh, A. (2010). A simple and rapid new dispersive liquid-liquid microextraction based on solidification of floating organic drop combined with inductively coupled plasma-optical emission spectrometry for preconcentration and determination of aluminium in water samples. *Journal of Hazardous Materials*, *178*(1–3), 766–770. doi: 10.1016/j.jhazmat.2010.02.006

Richards, L. A. (1931). Capillary conduction of uid through porous mediums. *Physics*, *Volume 1*, 318–333.

Ruecha, N., Rodthongkum, N., Cate, D. M., Volckens, J., Chailapakul, O., & Henry, C. S. (2015). Sensitive electrochemical sensor using a graphene-polyaniline nanocomposite for simultaneous detection of Zn(II), Cd(II), and Pb(II). *Analytica Chimica Acta*, *874*, 40–48. doi: 10.1016/j.aca.2015.02.064

Säbel, C. E., Neureuther, J. M., & Siemann, S. (2010). A spectrophotometric method for the determination of zinc, copper, and cobalt ions in metalloproteins using Zincon. *Analytical Biochemistry*, *397*(2), 218–226. doi: 10.1016/j.ab.2009.10.037

Sánchez Trujillo, I., Vereda Alonso, E., García de Torres, A., & Cano Pavón, J. M. (2012). Development of a solid phase extraction method for the multielement determination of trace metals in natural waters including sea-water by FI-ICP-MS. *Microchemical Journal*, *101*, 87–94. doi: 10.1016/j.microc.2011.11.003

Sethi, R., & di Molfetta, A. (2019). *Groundwater Engineering*. Springer.

Šimůnek, by J., Šejna, M., Saito, H., Sakai, M., & Th van Genuchten, M. (2013). *The HYDRUS-1D Software Package for Simulating the One-Dimensional Movement of Water, Heat, and Multiple Solutes in Variably-Saturated Media*.

Soodan, R. K., Pakade, Y. B., Nagpal, A., & Katnoria, J. K. (2014). Analytical techniques for estimation of heavy metals in soil ecosystem: A tabulated review. In Talanta (Vol. 125, pp. 405–410). Elsevier B.V. doi: 10.1016/j.talanta.2014.02.033

Sturgeon, R. E., Berman, S. S., Desaulniers, A., & Russell, D. S. (1979). Determination of Iron, Manganese, Zinc in Seawater by Graphite Furnace Atomic Absorption Spectrometry. *Analytical Chemistry*, *51*(14), 2364–2369. doi: 10.1021/ac50050a017

Tarboton, D. G. (2003). *RAINFALL-RUNOFF PROCESSES*. Retrieved from https://hydrology.usu.edu/rrp/

Tony, K., Rao, T., & Iyer, C. P. (1999). Flow injection on-line preconcentration and flame atomic absorption spectrometric determination of iron, cobalt, nickel, manganese and zinc in sea-water. *Analyst*, *124*(2), 191–195.

Tria, J., Butler, E. C. V., Haddad, P. R., & Bowie, A. R. (2007). Determination of aluminium in natural water samples. In Analytica Chimica Acta (Vol. 588, Issue 2, pp. 153–165). doi: 10.1016/j.aca.2007.02.048

Trujillo-González, J. M., Torres-Mora, M. A., Keesstra, S., Brevik, E. C., & Jiménez-Ballesta, R. (2016). Heavy metal accumulation related to population density in road dust samples taken from urban sites under different land uses. *Science of the Total Environment*, *553*, 636–642. doi: 10.1016/j.scitotenv.2016.02.101

Ulusoy, H. I., Gürkan, R., Aksoy, Ü., & Akçay, M. (2011). Development of a cloud point extraction and preconcentration method for determination of trace aluminum in mineral waters by FAAS. *Microchemical Journal*, *99*(1), 76–81. doi: 10.1016/j.microc.2011.03.013

van der Zee, S. E. A. T. M., & van Riemsdijk, W. H. (2059). Transport of Reactive Solute in Spatially Variable Soil Systems. In WATER RESOURCES RESEARCH (Vol. 23, Issue 11).

van Genuchten, M. T., & Nielsen, D. R. (1985). On describing and predicting the hydraulic properties. *Annales Geophysicae*, *3*(5), 615–628.

van Genuchten, M. Th. (1980). A Closed-form Equation for Predicting the Hydraulic Conductivity of Unsaturated Soils. *Soil Science Society of America Journal*, *44*, 892–898.

van Genuchten, M. Th., & Pachepsky, Y. A. (2011). Hydraulic properties of unsaturated soils. *Encyclopedia of Agrophysics*, 368–376.

Vukomanovic, D. v, Page, J. A., & Vanloon, G. W. (1991). Voltammetric determination of Al(111) with adsorptive preconcentration of the pyrocatechol violet complex. In Can. J. Chem (Vol. 69).

Wei, B., & Yang, L. (2010). A review of heavy metal contaminations in urban soils, urban road dusts and agricultural soils from China. In Microchemical Journal (Vol. 94, Issue 2, pp. 99–107). doi: 10.1016/j.microc.2009.09.014

Xia, L., Hu, B., Jiang, Z., Wu, Y., Li, L., & Chen, R. (2005). 8-Hydroxyquinoline-chloroform single drop microextraction and electrothermal vaporization ICP-MS for the fractionation of aluminium in natural waters and drinks. *Journal of Analytical Atomic Spectrometry*, *20*(5), 441–446. doi: 10.1039/b416938g

Zatta, P., Lucchini, R., van Rensburg, S. J., & Taylor, A. (2003). The role of metals in neurodegenerative processes: Aluminum, manganese, and zinc. In Brain Research Bulletin (Vol. 62, Issue 1, pp. 15–28). Elsevier Inc. doi: 10.1016/S0361-9230(03)00182-5

Zhao, L., Zhong, S., Fang, K., Qian, Z., & Chen, J. (2012). Determination of cadmium(II), cobalt(II), nickel(II), lead(II), zinc(II), and copper(II) in water samples using dual-cloud point extraction and inductively coupled plasma emission spectrometry. *Journal of Hazardous Materials*, *239–240*, 206–212. doi: 10.1016/j.jhazmat.2012.08.066

Appendix:
Characteristics of the used materials

Dorslilit n. 8 sand

Table A.1- Dorsilit n. 8 sand characteristics (from Dorfner data sheet)

CHEMICAL COMPOSITION	
SiO_2 ($\%_w$)	98
Al_2O_3 ($\%_w$)	0.8
Fe_2O_3 ($\%_w$)	0.01
TiO_2 ($\%_w$)	0.04
K_2O ($\%_w$)	0.3
Na_2O ($\%_w$)	0.03
CaO ($\%_w$)	0.02
MgO ($\%_w$)	0.01
PHYSICAL PROPERTIES	
Umidity ($\%_w$)	< 1
LOI (1000°c) ($\%_w$)	0.25
Density (g/mL)	2.63
Bulk density (g/mL)	1.6
Grain size (mm)	0.3-0.8
GRANULOMETRIC DISTRIBUTION	
> 0.8 (mm)	1
0.63 – 0.8 (mm)	37
0.315 – 0.63 (mm)	60
< 0.315 (mm)	2
d_{50} (mm)	0.57

LUFA Standard soil 2.2

Table A.2- Standard soil n. 2.2 characteristics according to GLP (modified from LUFA Speyer data sheet). All values are mean values of different batch analysis ± standard deviation. All values refer to dry matter

Organic carbon (% C)	1.77 ± 0.56
Nitrogen (% N)	0.20 ± 0.06
pH value (0.01 M $CaCl_2$)	5.6 ± 0.3
Cation exchange capacity (m_{eq}/100g)	8.5 ± 2.0
PARTICLE SIZE DISTRIBUTION (mm) according to German DIN (%)	
< 0.002	10.6 ± 1.9
0.002 – 0.006	3.3 ± 1.1
0.006 – 0.02	5.3 ± 0.5
0.02 – 0.063	7.4 ± 0.9
0.063 – 0.2	30.9 ± 3.4
0.2 – 0.63	41.6 ± 3.0
0.63 – 2.0	0.9 ± 0.1
Soil type	Loamy sand (lS)
PARTICLE SIZE DISTRIBUTION (mm) according USDA (%)	
< 0.002	10.6 ± 1.9
0.002 – 0.05	15.0 ±1.2
0.05 – 2.0	74.4 ±2.7
Soil type	Sandy loam
Maximum water holding capacity (g/100 g)	43.3 ±5.1
Weight per volume (g/1000 mL)	1224 ± 103

Gorno mine flotation rougher

Table A.3- WPPF Analysis results

Rwp, %	0.00
S	0.00
X^2	0.0000
Galena, syn	
Weight fraction, %w	1.53(19)
a, Å	5.93448
b, Å	5.93448
c, Å	5.93448
α, °	90.000
B, °	90.000
γ, °	90.000
Lattice volume, Å^3	209.001
Size, Å	0.0
Strain, %	0.21(9)
Calcite, syn	
Weight fraction, %w	9(2)
a, Å	4.98087
b, Å	4.98087
c, Å	17.07611
α, °	90.000
β, °	90.000
γ, °	120.000
Lattice volume, Å^3	366.885
Size, Å	0.0
Strain, %	0.058(4)

Table A.3- WPPF Analysis results (continue)

Sphalerite, Fe^{2+} bearing	
Weight fraction, %w	89(2)
a, Å	5.41101
b, Å	5.41101
c, Å	5.41101
α, °	90.000
β, °	90.000
γ, °	90.000
Lattice volume, Å^3	158.429
Size	0.0
Strain, %	0.099(8)
Cerrusite, syn	
Weight fraction, %w	0.71(8)
a, Å	5.21874
b, Å	8.52830
c, Å	6.06965
α, °	90.000
β, °	90.000
γ, °	90.000
Lattice volume, Å^3	270.142
Size, Å	0.0
Strain, %	0.14(9)

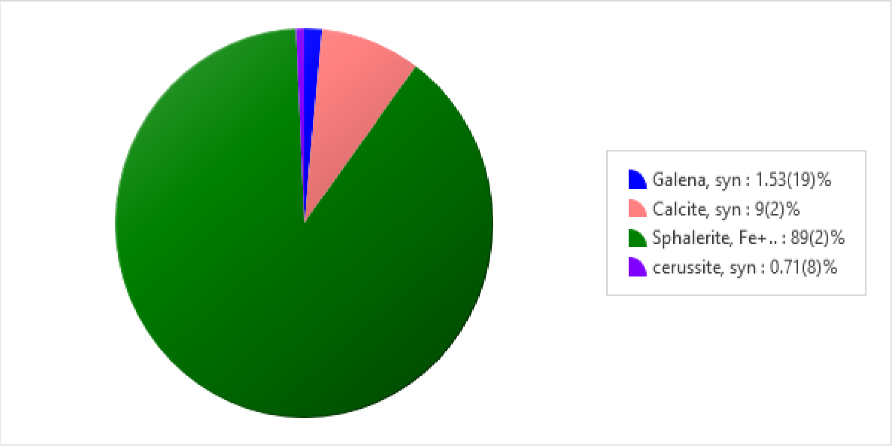

Figure A.4- WPPF weight fraction

Table 4.12- Measurement Conditions

X-Ray generator	40 kV, 30 mA	Scan mode	1D(scan)
Incident primary	Standard	Scan speed/Duration time	10.00 °/min
Goniometer	Standard Goniometer	Step width	0.01 °
Attachment	Standard attachment head	Scan axis	θ /2 θ
Filter	K β filter for Cu	Scan range	5 ~ 80 °
Selection slit	None	Incident slit box	2/3°
Diffracted beam mono	None	Length-limiting slit	10 mm
Detector	D/teX Ultra 2501	Receiving slit box #1	None
Optics attribute	BB	Receiving slit box #2	Open

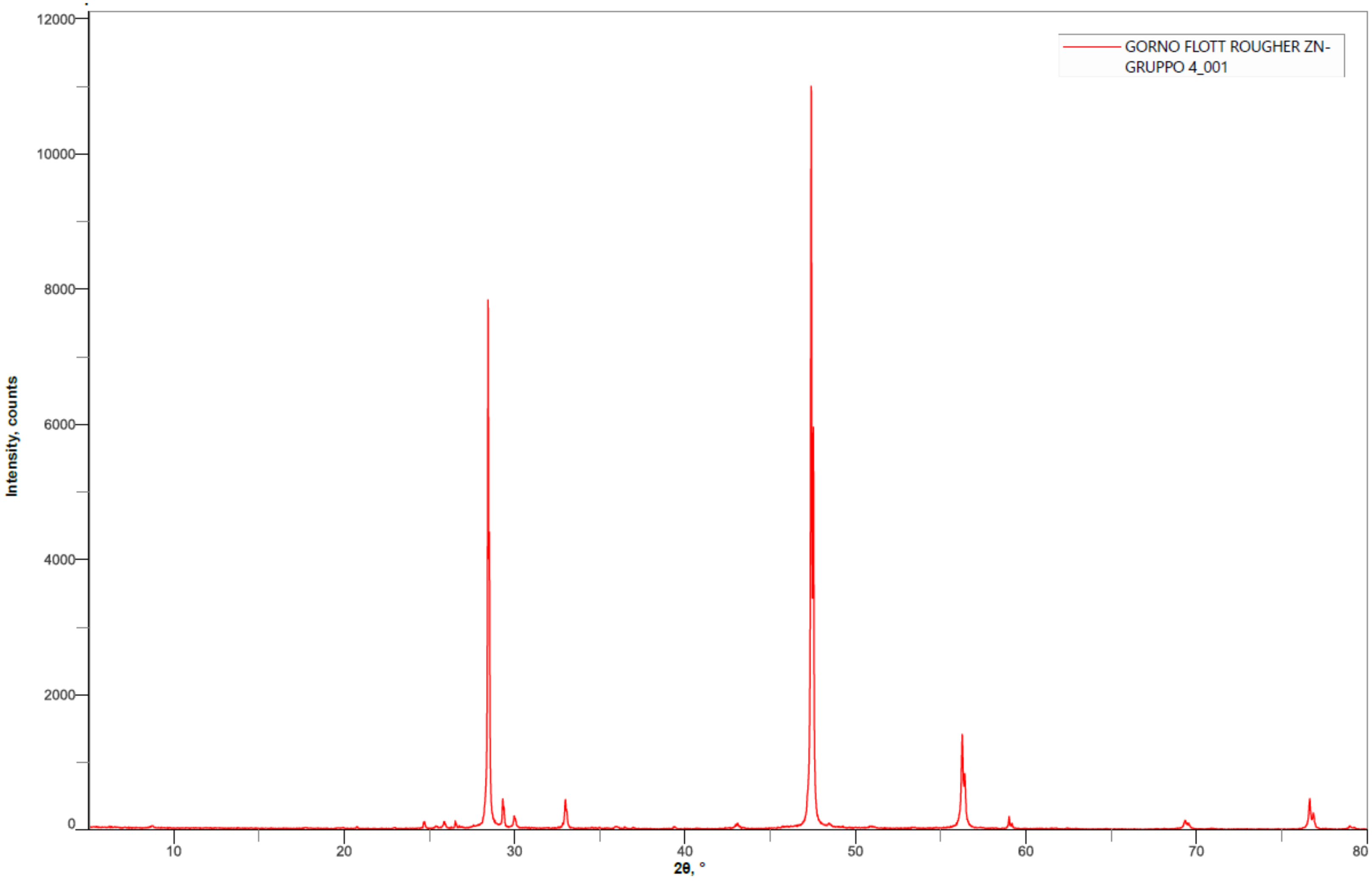

Figure A.5- *Measured profile view*

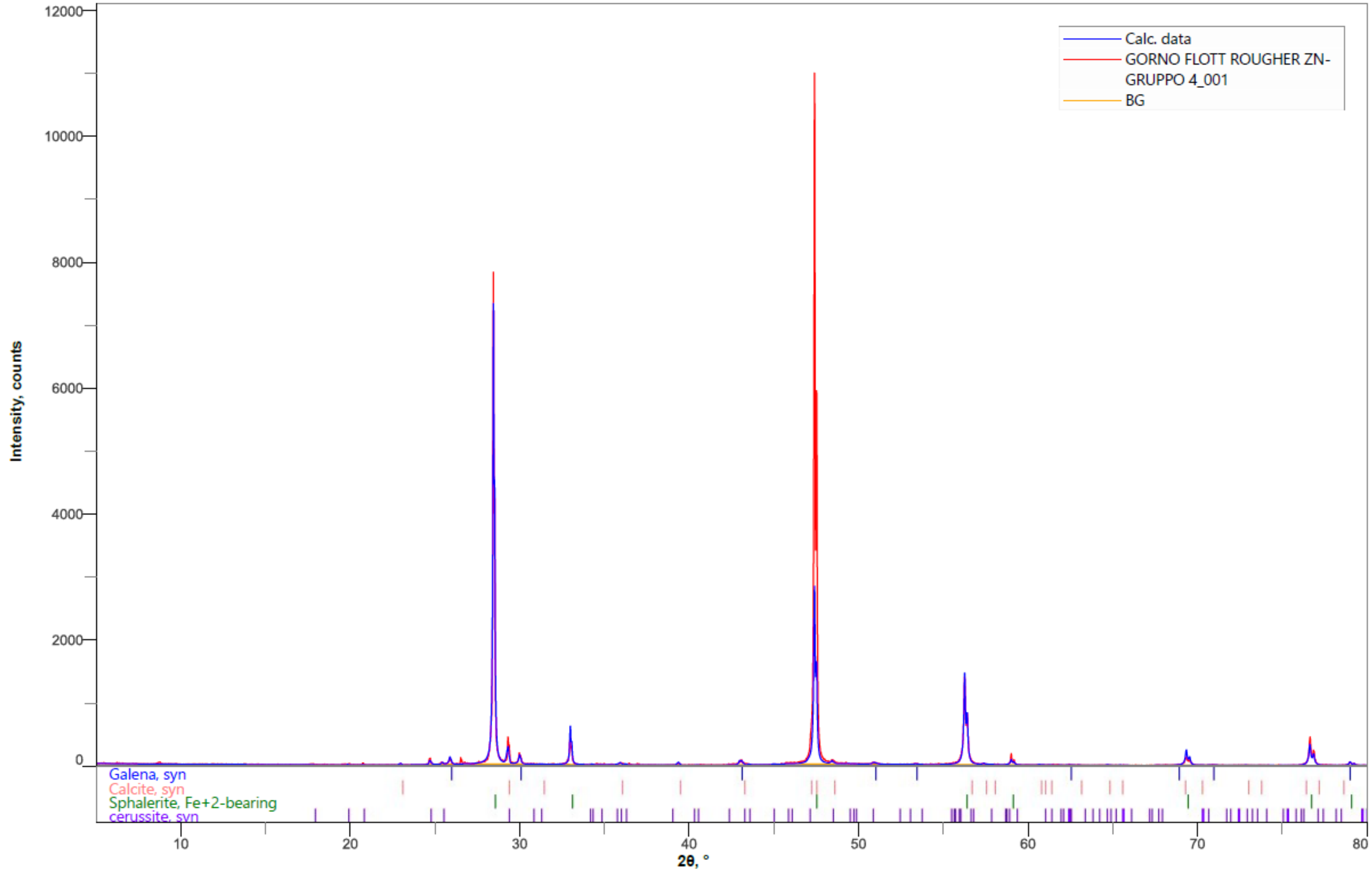

Figure A.6- WPPF Profile View

Acknowledgement

Firstly, thanks to all those who have participated to my thesis work.

Prof. Paola Marini and Ing. Oliviero Baietto for the site material and the analysis performed on it.

Prof. Tiziana Tosco, for being able to combine competence and humanity. She was always available for me, super timely in her replies.

I would like to sincerely thank Monica, for all the support during these months. With patience and competence, she introduced me to the magical lab world and became a point of reference to me.

A special thank goes to all the Groundwater Engineering group, you are amazing, guys! Between lunches and chat, I always felt at home with you and… I owe you many coffees!

Thanks to Mari, Bea, Fede and Lia, your friendship Is precious. These years wouldn't have been the same without you.

Thanks to Tiziana, my friend and 'bookish advice dealer'. Talking with you is a breath of fresh air.

Thanks to Lucilla, my old friend, for all the km you literally walked with me on summer evenings, talking about... the future.

The most important thank is for my parents. Mum and dad, thanks for being there, supportive and not judging. You helped me find the strength to go ahead when I couldn't.

Raffaele, my brother, deserves a particular thanks. Thanks for all the lightness and happiness you gave me, maybe even without knowing it.

Finally, I can't but thank who shared these years with me. Thanks for your support, in your way.

And even if it sounds awkward, I thank myself, my ups and downs, which give me the measure of how determined I can be.